

UC Irvine

UC Irvine Electronic Theses and Dissertations

Title

Machine Learning guided advanced Image Reconstruction in Photo Magnetic Imaging

Permalink

<https://escholarship.org/uc/item/7p76t431>

Author

Saraswatula, Janaki Sankirthana

Publication Date

2023

Peer reviewed|Thesis/dissertation

UNIVERSITY OF CALIFORNIA,
IRVINE

**Machine Learning guided Advanced Image Reconstruction
in Photo Magnetic Imaging**

DISSERTATION

Submitted in partial satisfaction of the requirements for
the degree of

MASTER OF SCIENCE

in ELECTRICAL AND COMPUTER ENGINEERING

by

Janaki Sankirthana Saraswatula

Thesis Committee:
Gultekin Gulsen, Ph.D, Chair
Terence Sanger, M.D
Glenn Healey, Ph.D

Supervisor:
Farouk Nouizi, Ph.D

2023

Table of Contents

A.	INTRODUCTION	8
B.	BACKGROUND	10
I.	Medical Imaging	10
II.	Diffuse Optical Imaging Techniques	11
1.	Fluorescence Tomography	11
2.	Diffuse Optical Tomography.....	11
III.	Photo Magnetic Imaging (PMI)	13
IV.	PMI Forward Problem.....	15
1.	Propagation of light in the tissue	15
2.	Propagation of heat in the tissue.....	16
3.	PMI forward Problem.....	16
4.	PMI Inverse Problem.....	17
C.	Background: Image Processing and Machine Learning	20
V.	Gray Level transformations in an Image.....	20
1.	Gray Level Thresholding.....	20
2.	Image Transformation functions	21
3.	Hough Space and Hough Transform	22
VI.	Machine Learning and Deep Learning.....	24
1.	Loss or Cost Functions	25
D.	Methodology	32
I.	PMI Data Generation	32
II.	Direct Detection Using Machine Learning	36
2.	Understanding the class imbalance and multilabel classification	37
III.	Region of Interest Localizer and Precision Improver	39
IV.	Precision Improvement	42
V.	The Testing procedure.....	43
VI.	Challenges	43
VII.	Preprocessing for Multi-Absorption Data.....	44

1.	Image Processing-based Global Pixel Transformations	44
2.	Drawbacks	45
3.	Minimum Enclosing Circle detection and Normalization	46
E.	Results and Discussion	47
VIII.	Representational Diagrams for Results	49
IX.	Results obtained using the ROI Network.....	51
X.	Results Obtained using ROI - Precision pipeline.....	52
1.	Predictions for a single absorption index	52
2.	Effect of absorption for Multi-Absorption Inclusions	54
3.	Effect of Size	56
4.	Effect of distance between inclusions with different contrasts	58
5.	Effect of distance for inclusions with the same absorption coefficient.....	60
F.	Conclusion and Future Work.....	61

List of Figures

Figure 1: The normalized absorption spectrum in the near-infrared spectral window are shown for water, lipid, oxy- and deoxyhemoglobin (Hb) [77-79]. As sensitivity to each chromophore concentration varies throughout the spectrum. The black arrows show representative wavelengths chosen to optimally recover the chromophores concentration in bio-tissue (760, 780, 830, 940 and 980 nm). 12

Figure 2: The PMI instrumentation: a) photography, b) schematic showing the laser beam irradiating a circular phantom (green). 14

Figure 3: The cross-section of representative MRT temperature maps obtained on: a) homogenous cylindrical phantom (μ_a), b) heterogeneous phantom bearing an inclusion with double the optical absorption of the phantom ($2\mu_a$). 14

Figure 4: The FEM mesh having 852 nodes, that is used to solve the PMI forward problem. 17

Figure 5: Step function used for thresholding transfer function at gray level 120. 21

Figure 6: Common gray level transformation functions [127]. 21

Figure 7: The position of x, y for a fixed radius $R = 5$ units for three different centers 23

Figure 8: The locus of points (a,b) for a fixed radius R . Their points of maximum intersection correspond to the centers of the circle in the x-y space. 23

Figure 9: Locus of points (a,b) for a variable radius R [130] 24

Figure 10: Plot of a straight line with slope = 1 and intercept =0..... 24

Figure 11: Representation of a Multi Output Linear Regression Model 25

Figure 12: Representative probability distribution of an outcome for an imbalanced binary classification task. 27

Figure 13: Comparison of Focal loss with Cross Entropy loss by varying γ [136]..... 28

Figure 14: Single-Layer Perceptron Model. 28

Figure 15: Multilayer perceptron network model. 30

Figure 16: Schematic representation of the PMI instrumentation setup..... 32

Figure 17: T2-weighted axial slice of a female rat showing the liver bearing: a) single, and b) double tumor as shown by the red arrows 33

Figure 18: Simulated temperature map obtained by solving the PMI forward problem on a homogeneous phantom ($\mu_a=0.01 \text{ mm}^{-1}$, $\mu_s'=0.86 \text{ mm}^{-1}$), that is heated using four illumination ports..... 33

Figure 19: Representative phantoms used to generate the training data. Schematic showing the inclusions containing a) a single node, single inclusion, and c) multiple inclusions. C_μ represent the contrast in absorption. d-f) Temperature maps obtained after 8 seconds of heating. g-i) Temperature maps showing the hot blobs at the hot nodes' location after subtraction of the homogeneous temperature map 35

Figure 20: MRT map of a phantom with two inclusions having a) the same contrast factor $C_{\mu}=1.75$. b) different contrast factors.	36
Figure 21: a) temperature map obtained after subtraction of homogeneous map from the simulated MRT containing cancerous inclusions, b) the grayscaled MRT map of size 256 x 256, c) FEM mesh showing the hot nodes belonging to the inclusions.	38
Figure 22: The CNN architecture for ROI identification in a grayscaled MRT map.	39
Figure 23: Multi-inclusion MRT with inclusions of different absorption coefficients. Division Kernel size used for region splitting here is 7x7.	40
Figure 24: Representative region splitting or division kernels used for ROI prediction, a) Schematic of the used phantom, grayscale temperature map showing division kernels corresponding to: b) 7x7, c) 15x15 and d) 31x31.	41
Figure 25: The final methodology developed for hot nodes detection from all MRT maps.	44
Figure 26: Gray level transformation functions used for image transformation and inclusion normalizing.	45
Figure 27: Minimum enclosing circle detection of inclusions in the MRT maps.	46
Figure 28: Shows the different region splitting sizes used in our Roi detection network.	47
Figure 29: a) MRT map of a single cancerous inclusion of diameter 4 mm and absorption coefficient 0.0165 mm^{-1} , b) the grayscaled temperature map, c) Results obtained from the ROI Precision pipeline.	49
Figure 30: a) the difference temperature map containing two inclusions of different radii 1.75 mm and 1.35 mm and absorption coefficients of 0.017 mm^{-1} and 0.0145 mm^{-1} , respectively. b) grayscaled temperature map, c) results obtained using ROI Precision pipeline with Hough Transform.	50
Figure 31: The absorption sensitivity curve a) IOU score as a function of absorption and b) Ground Truth Accuracy as a function of the absorption of Inclusion.	54
Figure 32: Surface plot showing accuracy as a function of absorption indices or coefficients in the multi-inclusion MRT map and the separation distance between them. The diameter of inclusions was set to 3 mm.	60

ACKNOWLEDGMENTS

I would like to express my sincerest gratitude to the following individuals who have supported me immensely throughout my Master's Thesis Research.

First and foremost, I would like to thank my advisor on this research, Dr. Farouk Nouzi, for his ever-constant and invaluable guidance and support. I thank him for taking a tremendous effort towards making me understand and appreciate the science of medical imaging. His expertise and encouragement have been instrumental in navigating the challenges faced in this cross-domain research project.

Secondly, I would like to express my sincerest thanks to Dr. Gultekin Gulsen for this incredible opportunity and the learning experience that I have received under his guidance.

I would also like to thank committee members, Dr. Glenn Healey for his ever-constant support in the field of Image Processing and Computer Vision and, Dr. Terence Sanger for his crucial insight into Machine Learning and Neural Networks, which has helped me greatly understand the nature of this problem.

I am also grateful to my colleague, Mr. Rajas Rajendra Pathare, for his expertise, feedback, and constant reinforcement of our collaboration. I thank him for his unwavering support and friendship during the challenging times of this thesis project.

Finally, I would like to thank my father, for nurturing a curious and research-hungry mindset in me, my mother for her constant care, love, and understanding, and my brother, for always being my source of inspiration and motivation throughout this journey of graduate studies in the United States. Their encouragement and belief in my abilities gave me the strength to persevere and succeed.

ABSTRACT

Photo Magnetic Imaging (PMI) is a novel laser-based optical imaging technique. PMI is used to identify diseased tissue based on its endogenous tissue contrast or using disease-targeting exogenous optical contrast agents. It was first developed at the Center for Onco Functional Imaging at the University of California, Irvine. Optical imaging techniques generally suffer from poor spatial resolution due to the high scattering of optical photons in tissue. PMI attempts to provide quantitatively accurate optical images with high spatial resolution. In this study, phantoms mimicking optical properties of tissue are utilized to explore the use of Machine learning techniques and Finite Element Methods to drive an AI-based reconstruction of PMI images. Our proposed methodology consists of hybrid deep learning and a machine learning pipeline that first identifies the inclusions in the phantoms representing cancerous lesions and finally delineates their boundaries. Our method was tested on a variety of inclusions' sizes, locations, and absorption coefficients and demonstrated high precision (above 95%) and Intersection Over Union Accuracies (above 85%) for the realizable test cases.

A. INTRODUCTION

In recent years, Machine Learning (ML) and Artificial Intelligence (AI) have witnessed a remarkable interest in industrial and research applications. With the advancements in computational power combined with autonomous capabilities, AI has emerged as a powerful tool to aid complex problem-solving in research. Medical Imaging has seen significant advancements in recent years. ML algorithms have proven effective in enhancing the accuracy and efficiency of diagnosis, treatment, and monitoring of diseases and reducing the risk of misdiagnosis. These advancements possess tremendous implications for patient care and research. This thesis will explore one such application of Machine Learning for a medical imaging technique called ‘Photo Magnetic Imaging’ (PMI). This technique was developed by researchers at the Center for Functional Onco-Imaging at the University of California, Irvine.

PMI is a novel non-invasive functional imaging technique that involves using near-infrared (NIR) lasers and Magnetic Resonance Imaging (MRI) to detect abnormalities in soft tissues. It is particularly effective for detecting the presence of tumors not detectable by other imaging modalities. Utilizing the high sensitivity of optical imaging and high resolution of MRI, PMI provides quantitatively accurate images with high spatial resolution. In PMI, Magnetic Resonance Thermometry (MRT) images are acquired dynamically while the tissue is lightly heated with laser light (~ 2 °C). Due to their higher hemoglobin concentration, cancerous lesions absorb the NIR photons more than healthy tissue, and hence warm up slightly higher compared to the surrounding normal tissue. The delineation of these cancerous regions is achieved using a dedicated PMI image reconstruction algorithm using mathematical models of photon migration and heat diffusion in tissue. It involves a minimization process, which is carried out to minimize the difference between the predicted temperature maps and the measured MRT maps.

In this thesis, we introduce a machine learning methodology that helps to assist the faster convergence of this minimization problem. It predicts a binary mask underlying the diffused heat signature of the cancerous lesion in the MRT maps. Our Machine Learning pipeline is a two-stage detection network called the Region of Interest Localizer and Precision Improver. The first stage of this pipeline employs a convolutional neural network to pick out the regions in the MRT maps which contain cancerous lesions. The second stage is a statistical regression model that creates the binary mask for the cancerous regions and therefore points to the sources of the heat signature corresponding to these lesions in the phantom.

Our methodology employs a Finite Element Method mesh to discretize the thermal images produced by the MRI to localize the sources of cancerous heat signatures. This methodology is designed to be versatile. The transferability of the method enables easy localization of heat signatures in thermal images of all types. It can find its applications in building diagnostics [1], firefighting [2], surveillance and security applications [3], and many more.

B. BACKGROUND

I. Medical Imaging

Medical Imaging has been one of the cornerstones of advancements in modern medicine. It has been the most integral and influential of technological advancements for the detection, diagnosis, monitoring, and treatment of medical conditions. The wide array of techniques in medical imaging has paved the way toward an enhanced understanding of the human body for medical professionals.

There are two main categories of medical imaging techniques, namely, invasive and non-invasive [4]. Invasive techniques involve the insertion of an instrument into the human body for capturing detailed internal information of the human body by the means of images or signals. These techniques are mainly targeted toward diagnosing and treating specific diseases and possess a higher risk of complications than their non-invasive counterparts. Examples of invasive procedures include Angiography, Endoscopy, etc. Non-Invasive medical imaging techniques [5] retrieve detailed, real-time functional and structural information about the internal organs of the human body without making any incisions. They have enabled medical professionals to retrieve high-resolution information about the internal structures of patients. Some examples of non-invasive medical imaging techniques include- X-Ray Imaging, CT scan, Magnetic Resonance Imaging, Positron Emission Tomography, Photo Acoustic Imaging, etc. Non-Invasive medical imaging can be further classified into two types, *i.e.*, Anatomical or Functional [6]. Conventional anatomical imaging modalities such as computed tomography (CT) and magnetic resonance imaging (MRI) provide detailed information about the structural details of tissues under study but they provide little insight into tumor physiology. Functional Imaging techniques such as fMRI, PET, and Optical Imaging Techniques excel at providing the tissue or in the case of a cancerous lesion, the tumor's biological functions and the surrounding microenvironment. They usually provide high sensitivity and specificity but are limited by their poor spatial resolution and inability to provide anatomical detail. Continued advances in instrumentation and imaging agents development will improve our ability to noninvasively characterize disease processes.

II. Diffuse Optical Imaging Techniques

Diffuse Optical Imaging is a technique that employs light to retrieve functional information of the tissue under study. Optical imaging techniques have seen a rise in recent years due to their promise of providing an increased functional contrast allowing the investigation of key biological parameters of the tissue and diagnosing any unhabitual physiological anomalies. Typically, near-infrared (NIR) light, in the range of 600-1000 nm is used to illuminate the tissues due to its low attenuation that allows deep penetration [7].

1. Fluorescence Tomography

Fluorescence imaging is based on the detection of fluorescence light emitted by dyes or proteins when excited by a specific wavelength of light [8-12]. Fluorescence tomography (FT) uses the principles of fluorescence imaging to create three-dimensional (3D) images of the distribution of these dyes or proteins within the imaged biological samples. FT utilizes multiple measurements from different sides of the sample to reconstruct the 3D images, rather than a single two-dimensional (2D) projection image [13-46].

When using exogenous contrast agents, the fluorescent dye is first injected into the sample. After the accumulation of a portion of the dye in specific tissue areas, the sample is then excited by a light source, typically a laser, which causes the fluorescent dye to emit fluorescent light. The emitted light is then collected by detectors placed around the sample at different angles. The tomographic data is then used to reconstruct a 3D image of the distribution of the dye within the sample using dedicated image reconstruction algorithms. FT has several advantages such as its ability for the non-invasive visualization of fluorescent-labeled biomolecules, which can provide new insights into the functional physiology of various organs and tissues. Additionally, FT can provide functional information in real-time, making it a powerful tool for both research and clinical applications [34, 35, 47-54]. It has been used to study a wide range of biological processes and diseases such as cancer [42]. It has also been used to study the distribution of drugs and other therapeutic agents in the body, which can help to optimize treatment regimens. FT is still a relatively new technology and remaining some challenges need to be overcome before its widespread in the clinic. Indeed, its widespread has been hampered by its low spatial resolution and the availability of only few FDA-approved fluorescent dyes.

2. Diffuse Optical Tomography

Diffuse Optical Tomography (DOT) utilizes NIR light to probe tissues and retrieve functional information [55, 56]. NIR light travels several centimeters through the tissue

under study, experiencing absorption and scattering, thus exponentially attenuating its intensity as a function of its distance from the source [57]. The attenuated light is then measured by detectors positioned around the boundary of the tissue [58-62]. If the light sources and detectors are placed on the same side of the boundary, the DOT is said to be in reflectance mode; if placed on the opposite sides of the tissue, it is in transmission mode. DOT provides 3D distribution of the optical properties of the tissue using the measured optical signals. An image reconstruction algorithm iteratively minimizes the difference between the data measured directly from the tissue at the detector and the synthetic ones generated using mathematical models of the propagation of light in tissue [63-66]. Generally, this modeling is performed using the diffusion equation [67-70].

The introduction of multiwavelength DOT enabled the recovery of further functional information from tissues such as total hemoglobin concentration and oxygen saturation by recovering the tissue chromophore concentrations [71-76]. The tissue absorbs light differently at different wavelengths. This characteristic is modeled using the absorption spectrum of the tissue. Therefore, photons of a specific energy or wavelength shall be absorbed by the tissue more than others. When NIR light is shone on the tissue, its chromophores such as hemoglobin, water, and lipids differently absorb it. Assessing the concentration of these endogenous chromophores is essential to understand and tracking different biological processes of the tissue. Their concentrations change in response to different abnormalities in the tissue and thus can be used as biomarkers. Their different absorption is usually described by their absorption spectra as shown in Fig.1

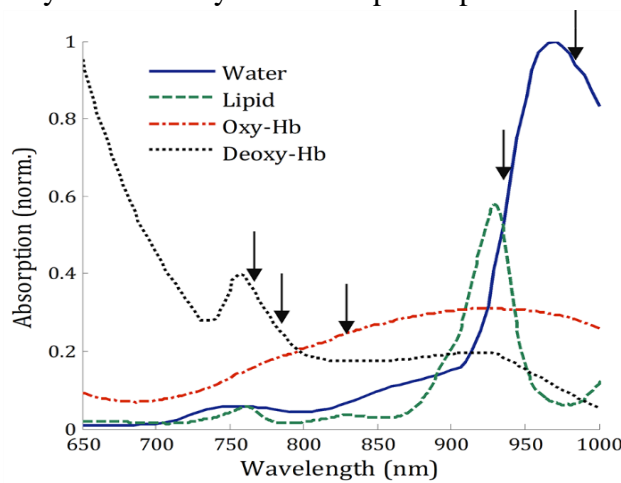


Figure 1: The normalized absorption spectrum in the near-infrared spectral window are shown for water, lipid, oxy- and deoxyhemoglobin (Hb) [77-79]. As sensitivity to each chromophore concentration varies throughout the spectrum. The black arrows show representative wavelengths chosen to optimally recover the chromophores concentration in bio-tissue (760, 780, 830, 940 and 980 nm).

The absorption coefficient of a medium at wavelength λ can be calculated as the sum of the absorption coefficients of its chromophores. The chromophores' concentration C can

be recovered using the total absorption coefficient $\mu_a(\lambda)$ and the extinction coefficient $\varepsilon(\lambda)$ at that wavelength using the modified Beer-Lambert's law [57, 79-81]:

$$\mu_a(\lambda) = \log \sum_{i=1}^{N_c} \varepsilon_i(\lambda) \cdot C_i \quad (1)$$

Where N_c is the number of chromophores considered in the experiment.

DOT has several advantages since it is non-invasive and does not use ionizing radiation, which makes it a much safer imaging technique that can be used frequently *in vivo*. For example, it has been widely used as a low-cost clinical research tool of special importance in breast cancer [25, 79, 82-86].

However, the widespread of DOT in the clinic has been delayed due to its limited spatial-resolution (~ 7 mm). This is mainly due to the important scattering of light photons in the medium during their propagation. This makes the DOT inverse problem, ill-posed and highly undetermined [87-89]. Considerable efforts have been made to overcome these limitations. One of which is the combination of DOT with high-resolution anatomical imaging modalities to improve its spatial-resolution [28, 64, 68, 69, 90-96]. Unfortunately, this approach remained limited to using the structural information to constrain the image reconstruction algorithm of DOT. As an effort to overcome these limitations, the Center for Functional Onco-Imaging at the University of California, Irvine has introduced a novel diffuse optical technique termed Photo Magnetic Imaging (PMI) [97-99].

III. Photo Magnetic Imaging (PMI)

The PMI technique was developed to overcome the ill-posed nature of DOT. PMI combines optical and magnetic resonance imaging (MRI) to provide high-resolution optical absorption maps. It leverages the high sensitivity of optical imaging and the high resolution of MRI. Nevertheless, PMI is not based on the standard combination of these two modalities but proposes a novel scheme to employ them synergically. In PMI, the tissue under study is illuminated by NIR lasers to induce a temperature increase while being monitored by magnetic resonance thermometry (MRT), Fig 2.

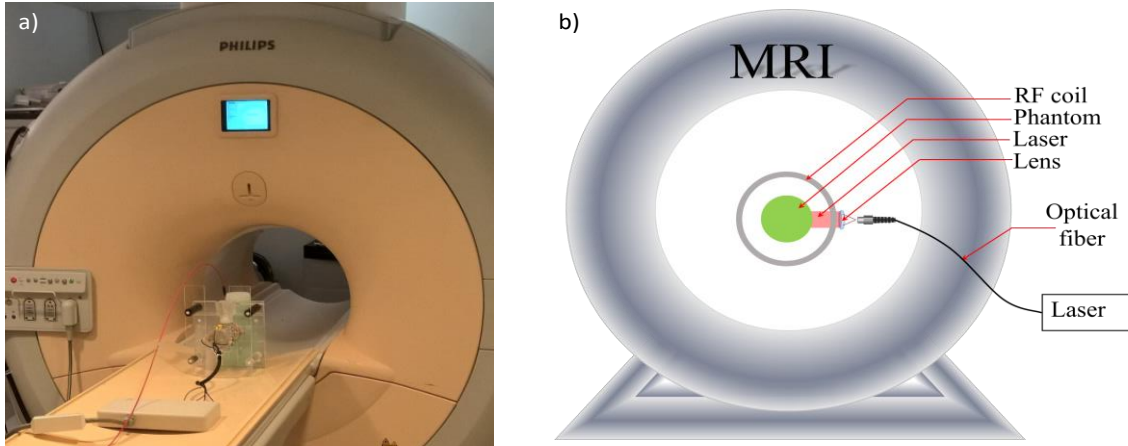


Figure 2: The PMI instrumentation: a) photography, b) schematic showing the laser beam irradiating a circular phantom (green).

The internal increase in temperature is proportional to both the absorption coefficient of the medium as well as the intensity of the incident laser beam. Indeed, when the laser beam illuminates the tissue under study, photons are locally absorbed by the medium. This energy absorbed from the photons is converted into bio-heat by the tissue. Figure 3 shows the cross-section of representative MRT temperature maps obtained on: a) a homogenous cylindrical phantom, b) a heterogeneous phantom bearing an inclusion with double the optical absorption of the phantom.

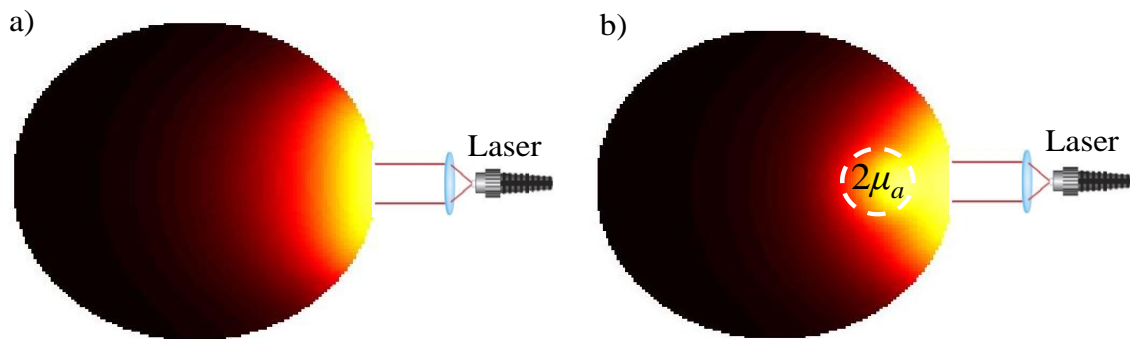


Figure 3: The cross-section of representative MRT temperature maps obtained on: a) homogenous cylindrical phantom (μ_a), b) heterogeneous phantom bearing an inclusion with double the optical absorption of the phantom ($2\mu_a$).

As can be seen in figure 3. b, the additional increase in temperature at the inclusion location is only due to its higher absorption since all experimental parameters were kept the same for results in figure 3. a and 3. b.

IV. PMI Forward Problem

1. Propagation of light in the tissue

The propagation of light in the biological tissue can be modeled by the Boltzmann transport equation, also known as the radiative transfer equation (RTE) [100]. Resolving RTE to model light propagation is very time-consuming. Thus, this modeling is often performed using its approximated version called the diffusion equation (DE). The use of the diffusion equation is valid when scattering is dominant in the medium and requires the source-detector separation to be larger than the scattering mean free path [28]. The diffusion equation is given by [66, 87, 88, 101]:

$$S(\mathbf{r}) = -\nabla \cdot [D(\mathbf{r})\nabla\phi(\mathbf{r})] + \mu_a(\mathbf{r})\phi(\mathbf{r}) \quad (2)$$

Where $S(\mathbf{r})$ is the isotropic light source, $\phi(\mathbf{r})$ is the direction-independent photon density, $D(\mathbf{r})$ is the diffusion coefficient and μ_a is the absorption coefficient. The diffusion coefficient $D(\mathbf{r})$ as a result of both absorption and scattering is the reciprocal of the weighted sums of the absorption (μ_a) and reduced scattering coefficient (μ'_s) given as

$$D(\mathbf{r}) = \frac{1}{3(\mu_a(\mathbf{r}) + \mu'_s(\mathbf{r}))} \quad (3)$$

The Robin Boundary Condition which relates the photon flux and photon density to obtain the photon density at the surface of the tissue is used:

$$-D(\mathbf{r})\nabla\phi(\mathbf{r}) \cdot \mathbf{n} = \frac{\phi(\mathbf{r})}{2A} \quad (4)$$

Where \mathbf{n} is the vector normal to the surface, A is the index mismatch parameter caused due to internal boundaries with different refractive indices and is related to the internal reflection coefficient R and refractive index η by:

$$A = \frac{1+R}{1-R}; \text{ and } R = -1.4399\eta^{-2} + 0.7099\eta^{-1} + 0.6681 + 0.0636\eta \quad (5)$$

2. Propagation of heat in the tissue

We can model the temperature increase in the medium as a function of space and time using the photon density obtained from the diffusion equation using the Pennes bioheat equation [102-104].

$$Q_s = \rho c \frac{\partial T(r,t)}{\partial t} - \nabla[k\nabla T(r,t)] \quad (6)$$

Here Q_s is the NIR laser-induced heating source, ρ is the density, c is the specific heat, T is the temperature of the tissue at position r and time t . k is the thermal conductivity of the tissue.

3. PMI forward Problem

The resolution of the PMI forward problem consists in simulating the temperature increase and propagation within a medium illuminated with a laser knowing its power and the medium optical properties. It is generally obtained using Finite Element Method (FEM) to provide a numerical solution for the combined diffusion (Eq.2) and heat equations (Eq.6). FEM is based on the discretization of the medium, using a FEM mesh. This mesh is composed of non-overlapping triangles in 2D and tetrahedral elements for 3D. The intersection points of these triangular elements are called mesh *nodes*.

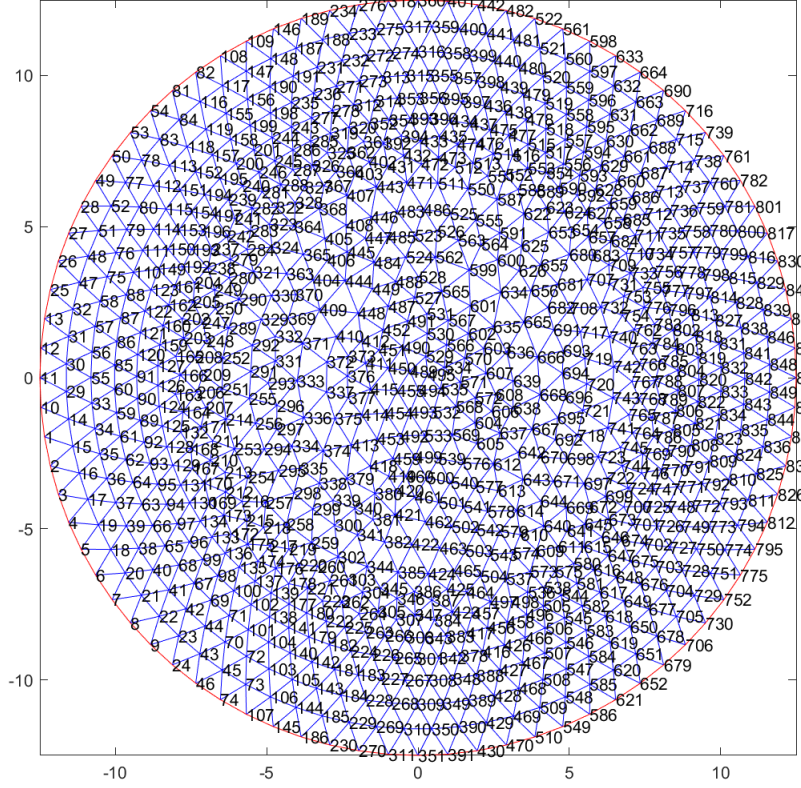


Figure 4: The FEM mesh having 852 nodes, that is used to solve the PMI forward problem.

4. PMI Inverse Problem

The resolution of the PMI inverse problem allows to recover the absorption values at each node of the FEM mesh using the internal MRT temperature measurements. These absorption maps are recovered by iteratively minimizing the least square error between the measured temperature map and the simulated map obtained by assuming an absorption value μ_a given as [105-116]:

$$\Omega(\mu_a) = \operatorname{argmin}_{\mu_a} \sum_{n=1}^N (\Gamma_n - T_n(\mu_a))^2 \quad (7)$$

Where N is the number of the FEM nodes, Γ_n is the measured temperature map and T_n is the simulated temperature map.

The absorption coefficient μ_a is iteratively updated by minimizing Eq.7 using the Levenberg–Marquardt algorithm as follows [105]:

$$\Delta\mu_a = (J^T J + \alpha I)^{-1} J^T (\Gamma_i^m - T_i)^2 \quad (8)$$

Where $\Delta\mu_a$ is the update at each iteration i of the minimization process, α is the regularization parameter. The μ_a that produces the smallest error between the simulated and measured temperature maps is chosen to be the final PMI absorption coefficient map. J is the sensitivity matrix or the Jacobian Matrix. J is a matrix describing the influence of the variation of the absorption coefficient at given nodes on the induced temperature variations at all nodes [18]:

$$J = \begin{bmatrix} \frac{\partial T_1}{\partial \mu_{a1}} & \dots & \frac{\partial T_1}{\partial \mu_{aN}} \\ \vdots & \ddots & \vdots \\ \frac{\partial T_N}{\partial \mu_{a1}} & \dots & \frac{\partial T_N}{\partial \mu_{aN}} \end{bmatrix} \quad (9)$$

The minimization process described by Eq.8 results in images with poor spatial resolution and quantitative accuracy. Several research groups attempted to enhance the spatial resolution of diffuse optical imaging. One solution consisted in combining optical imaging with structural imaging, which has higher spatial resolution [8, 9, 15, 16, 63, 90-94, 117-121]. Therefore, the update to the optical absorption unknown μ_a is achieved with:

$$\Delta\mu_a = (J^T J + \alpha L^T L)^{-1} J^T [T^m - T(\mu_a)] \quad (10)$$

Where L is a penalty matrix built using the binary mask retrieved from the anatomical structural information. The penalty matrix L can be obtained as follows [23, 95, 122]:

$$L_{ij} = \begin{cases} 0 & \text{i and j not in the same region} \\ -\frac{1}{N_r} & \text{i and j in the same region} \\ 1 & i = j \end{cases} \quad (11)$$

Where N_r represents the number of nodes included in each region r . Unfortunately, this approach was also demonstrated to be limited due to the mismatch between the functional and structural information within the body. At the Center for Functional Onco-Imaging at UCI, our team introduced two novel methodologies that bring functional and anatomical imaging techniques to work synergically. These novel imaging modalities termed Temperature Modulated Fluorescence Tomography (TMFT) [14, 17-21, 23, 27, 123-126] and PMI [103-116] utilize both imaging modalities to induce or measure changes caused by the propagation of light within the medium. In PMI, which is the technique of interest in this work, information about the presence of higher absorbing regions can be directly extracted from the MRT-measured temperature maps before any reconstruction process. Unlike standard *a priori* anatomical information, these regions directly match the regions

of interest to be later reconstructed by the PMI algorithm. However, due to temperature diffusion, the observed regions are diffused and are typically larger than the region to be reconstructed.

C. Background: Image Processing and Machine Learning

I. Gray Level transformations in an Image

Spatial image enhancement is a process where a function t is applied to a neighborhood $n(x, y)$ around every pixel $p(x, y)$ of an image $f(x, y)$ to obtain a transformed image $g(x, y)$ given by the following equation:

$$g(x, y) = t(n(x, y)) \quad (12)$$

n is usually a square or a rectangular region centered around the pixel $p(x, y)$. When the neighborhood size $N = 1$, this transformation is called the gray level transformation. If 'r' is the gray level at the location (x, y) of the input image, the corresponding transformed gray level at (x, y) in the output is given as s , which is given by the following equation:

$$s = T(r) \quad (13)$$

1. Gray Level Thresholding

The transformation function used in thresholding of images is a step function, given as follows:

$$g(x, y) = \begin{cases} A; & f(x, y) \geq T \\ B; & f(x, y) < T \end{cases} \quad (14)$$

Where $g(x, y)$ is the transformed image, $f(x, y)$ is the input image and T is the threshold gray value. A and B are the new values of the pixel intensity at a given location (x, y) in the image after the thresholding operation.

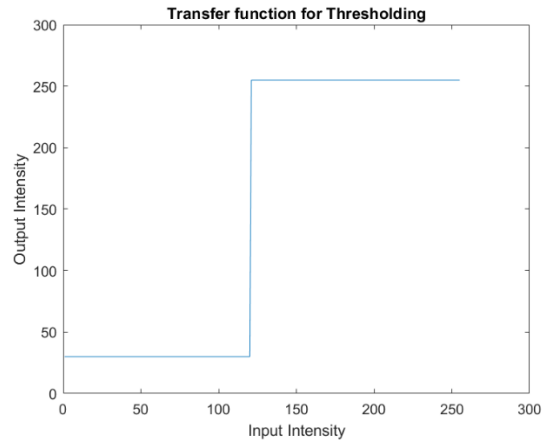


Figure 5: Step function used for thresholding transfer function at gray level 120.

Thresholding is a common technique used to segment images, *i.e.*, separation of objects of interest and background for feature extraction from images.

2. Image Transformation functions

The following figure depicts the different image transformation functions that are commonly used in image processing.

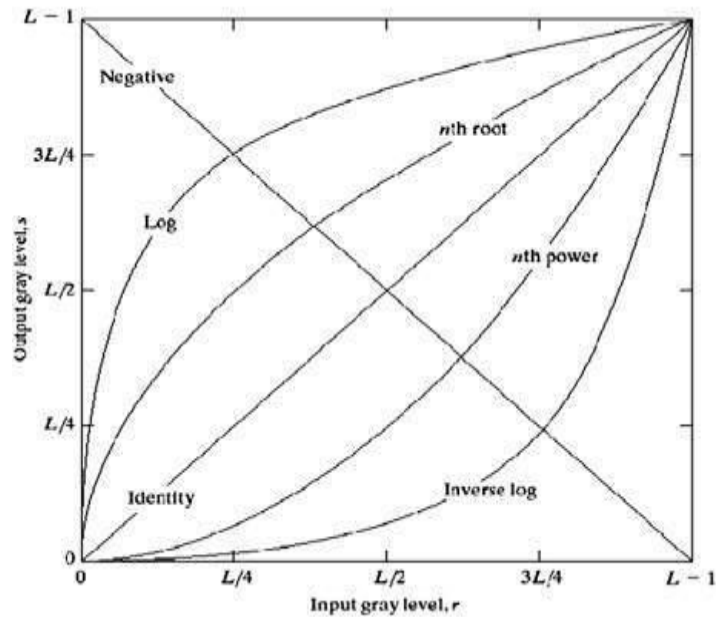


Figure 6: Common gray level transformation functions [127].

3. Hough Space and Hough Transform

The Hough transform as it is in use today was first proposed by R. Duda and P. Hart [128], then was popularized in the computer vision community by D. H. Ballard [129]. The Hough Transform algorithm is a feature extraction technique, which is used to detect and extract objects of interest from an image once the class of shapes to be extracted is specified. The most common objects of interest extracted using the Hough transform are lines, curves, and by extension circles, ellipses, etc.

A usually imperfect object is determined as a region of interest in the image by a mechanism of voting in a special parametric space known as the “Hough Space”. The parametric equations of a circle of Radius R and center (a, b) is given as follows:

$$\begin{cases} (x - a)^2 + (y - b)^2 = R^2 \\ x = a + R \times \cos \theta \\ y = b + R \times \sin \theta \end{cases} \quad (15)$$

Where θ is the sweeping angle made by the points (x, y) , which are on the boundaries of the circle.

Then, the task is to find image points that fall on the boundaries of the circles described by the coordinates (a, b, R) for each circle. These points are obtained by taking the gradient of the input image to retain only those pixels which correspond to the boundaries of the circles in the image. We limit our search space by constraining the radius of the circle. If we assume that the radius R of the circle is known, our search space is limited to the pair (a, b) . The circles shown in the below image are of the chosen radius but are centered at different positions in space. We now search in the (a, b) space for parameters that satisfy the following condition:

$$\begin{cases} a = x - R \times \cos \theta \\ b = y - R \times \sin \theta \end{cases} \quad (16)$$

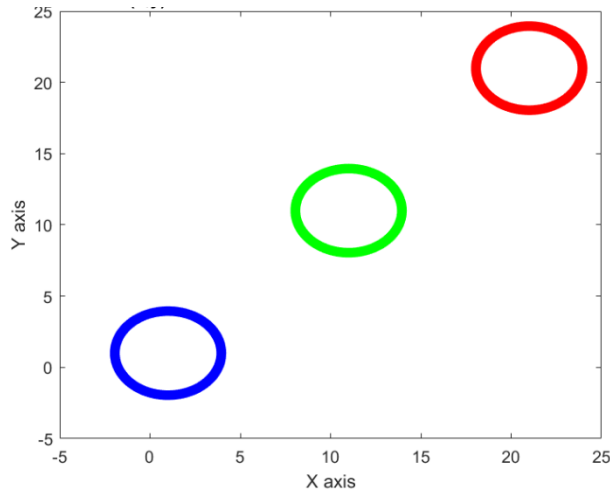


Figure 7: The position of (x, y) for a fixed radius $R = 5$ units for three different centers

The locus of the points (a, b) in the parameter space is a circle of the fixed radius R centered at (x, y) . A hough accumulator array is an array described by (a, b, R) . For each image point (i, j) that may lie on a circle, we increment all cells for which according to

$$(i - a)^2 + (j - b)^2 = R^2 \quad (17)$$

It could be the center of the circle. Then we search for a local maximum on the hough accumulator array.

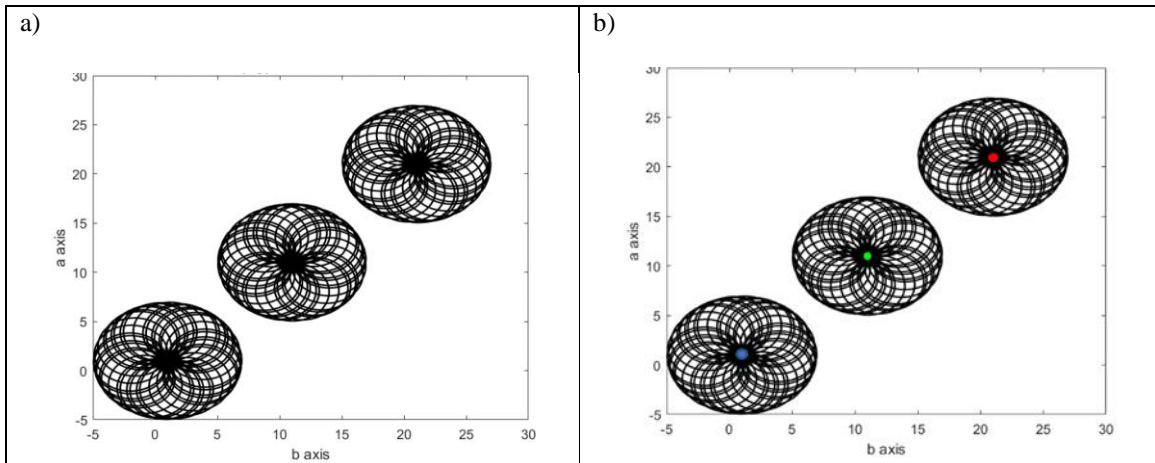


Figure 8: The locus of points (a, b) for a fixed radius R . Their points of maximum intersection correspond to the centers of the circle in the x - y space.

If the radius of the circles in the image is not known beforehand, then the locus of the points in the (a, b) space shall fall on the surface of a cone. Each point (x, y) will produce a cone

as described by the 3D parametric space (a,b,R) and the local maxima of the intersection of these cones shall correspond to our potential circles in the input image.

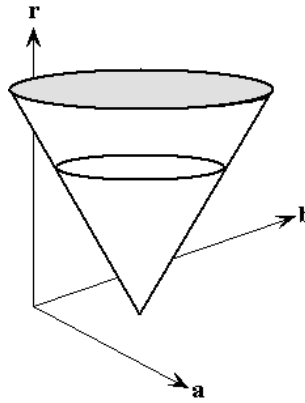


Figure 9: Locus of points (a,b) for a variable radius R [130]

II. Machine Learning and Deep Learning

Linear Regression is a statistical machine learning (ML) methodology that fits a line, also known as the ‘best-fit line’ through data points [131, 132]. The equation for the best-fit model in the case of a single input single output model is given as:

$$y = mx + c \quad (18)$$

Where y is the output of the regression model or the response of the ML model, x is the input data or the input signal, m is the slope, and c is the bias of the line, given in the figure below.

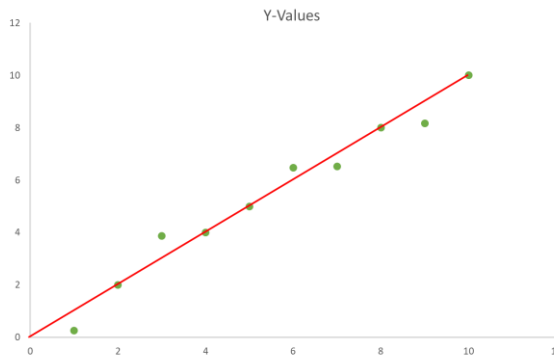


Figure 10: Plot of a straight line with slope = 1 and intercept =0

For multi-output prediction [133], where we have P outputs for a given input, the output vector y is a $P \times 1$ vector. If x is an $M \times 1$ dimensional vector, the weight vector connecting the output to the input is a matrix of shape $M \times P$, as shown in Figure 11.

Finding the output of the regression model consists in updating the weights of the model such that the squared error between the calculated or predicted response and desired response is minimized, also called the least square minimization. The performance of a regression model is determined by its R^2 score given as:

$$R^2 = 1 - \frac{\text{Sum of Square of Residuals}}{\text{Total Sum of Squares}} \quad (19)$$

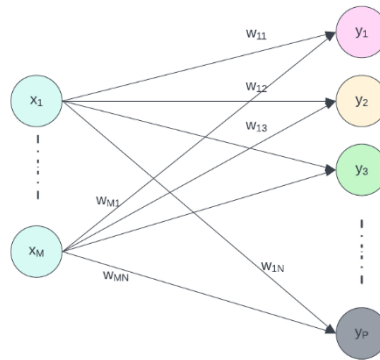


Figure 11: Representation of a Multi Output Linear Regression Model

1. Loss or Cost Functions

Cost functions or Loss functions determine the performance of a model in ML. Through Cost Functions, we can provide a mathematical representation of the objectives of the learning task. Below is a list of some of the cost functions used for the task of classification [134].

Entropy of a Random Variable

Entropy is a measure of randomness in the values taken by the variable in an experiment. The larger the value of the entropy, the more randomness in the variable. It also measures the number of bits required to represent a random variable. The entropy of a random variable X is given as:

$$H(X) = \sum_x p(x) \cdot \log(p(x)) \quad (20)$$

Where x is a sample value taken by the variable X and $p(x)$ is the probability of the occurrence of x .

Cross Entropy

Cross Entropy measures the difference between probability distributions. It also represents the number of bits required to project the variable from one distribution to another:

$$H(y, \hat{y}) = -\sum_i y_i \cdot \log(\hat{y}_i) \quad (21)$$

where y is the probability of a sample from distribution 1 and \hat{y} is the probability of a sample from distribution 2.

The Cross-Entropy metric is used as a loss function in classification tasks as it calculates the difference between the measured and the true probability distributions [135]. A learning model generally aims to minimize the difference between these probability distributions.

Binary Cross Entropy

Since cross-entropy is a distribution-based loss function, it is derived from the distribution of the outputs or 'labels'. In binary classification, the outputs take only two values, 0 or 1, and the loss function is derived assuming a Bernoulli distribution of the outputs, *i.e.*, the probability of the variable assuming the value of '0' is exactly equal to '1'. Therefore, the equation of Cross Entropy becomes:

$$L_{CE}(y, \hat{y}) = -(y \cdot \log \hat{y} + (1 - y) (\log 1 - \hat{y})) \quad (22)$$

Where y is the true output and \hat{y} is the output predicted for a given input by the ML model.

Weighted Cross Entropy (WCE)

The WCE loss function is used when the output distribution to be approximated is skewed, and when the probabilities of the occurrence of each of the outcomes by the random variable are unequal, as shown in Figure 12. In Eq. 23, the parameter β makes the learning model more attuned to false positives if it assumes a value less than 1, and to false negatives if it takes a value greater than 1.

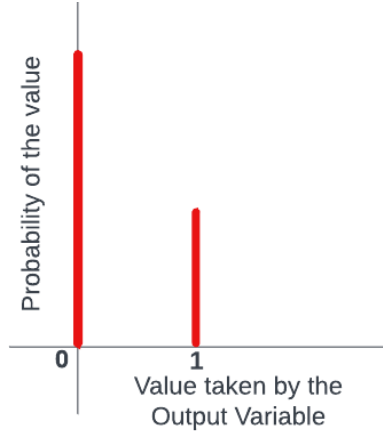


Figure 12: Representative probability distribution of an outcome for an imbalanced binary classification task.

$$L_{WCE}(y, \hat{y}) = -(\beta \cdot y \cdot \log \hat{y} + (1 - y) (\log 1 - \hat{y})) \quad (23)$$

Balanced Cross Entropy (BCE)

Balanced Cross Entropy is also used as a loss function that is more suited for imbalanced datasets. Weights are assigned to both the positive and negative classes such that the sum of the weights add to one, given as:

$$L_{BCE}(y, \hat{y}) = -(\beta \cdot y \cdot \log \hat{y} + (1 - \beta)(1 - y) (\log 1 - \hat{y})) \quad (24)$$

Focal Loss

The expression for Focal loss is given as:

$$L_{FL}(p_t) = -\zeta^t (1 - p_t)^\gamma \log p_t \quad (25)$$

Where p_t is the estimated probability distribution of the output variable. The factors γ and ζ work together to down weight the contribution of easy-to-classify examples. The value of γ controls the shape of the curve and reduces the loss for well-classified examples with high ground truth probability shown in Fig 13. But the function produces a high loss for poorly classified examples, in turn forcing the gradient descent to reduce the high loss produced for these classes of examples.

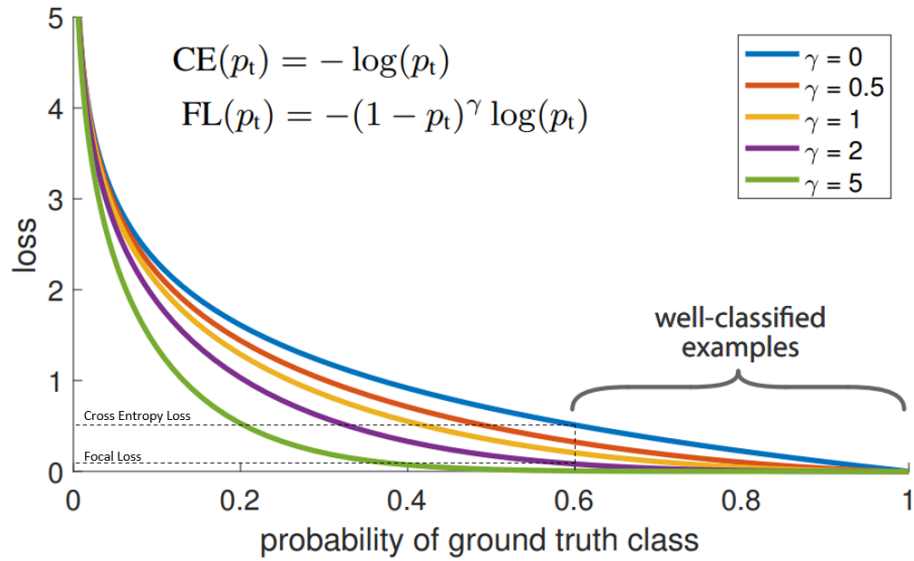


Figure 13: Comparison of Focal loss with Cross Entropy loss by varying γ [136].

Multilayer Perceptron Networks or Neural Networks

Single-layer perceptron model

In the domain of deep learning, the most rudimentary and fundamental model is the Perceptron model, first proposed by F. Rosenblatt [131, 137]. The following figure showcases a single-layer perceptron model.

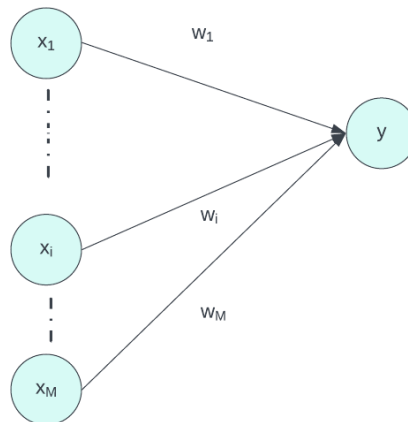


Figure 14: Single-Layer Perceptron Model.

The data vector X is fed into the network using the input layer, which contains the same number of neurons as the length of a data point in the input vector space. Each neuron or ‘node’ of the input layer is connected to every node of the intermediate or the hidden layer,

so called because the computations remain hidden inside the structure of the model. The input layer is connected to the neurons of the hidden layer through linear combinations. If the datapoint x_i in the i^{th} neuron of the input layer is connected to the output neuron by a weight w_i , the output of perceptron network is given as:

$$y = f(\sum_i x_i \cdot w_i) \quad (26)$$

Or

$$y = f(w^T x) \quad (27)$$

Where f is the activation function applied to the linear combination output to introduce non-linearity into the network. In the Rosenblatt perceptron model, the activation function is the threshold or step function given by:

$$y = \begin{cases} 0 & ; \text{if } w^T \cdot x \leq \kappa \\ 1 & ; \text{if } w^T \cdot x > \kappa \end{cases} \quad (28)$$

Where κ is the threshold chosen for the network.

Learning Rule of a Perceptron

The output of the perceptron is calculated and compared with the true output associated with the input data. An error is calculated and this error in the model prediction is used to update the free parameters or the tunable parameters of the model, *i.e.*, the weights and biases of the network. Error in the prediction by the network is given by:

$$error = e(y, \hat{y}) = y - \hat{y} \quad (29)$$

And the weight update rule is given by:

$$w(t + 1) = w(t) + \eta(e(y, \hat{y})) \quad (30)$$

Where η is the learning rate of the model, which determines the effect of the error on the weights of the perceptron model.

Multi Perceptron Networks or Neural Networks

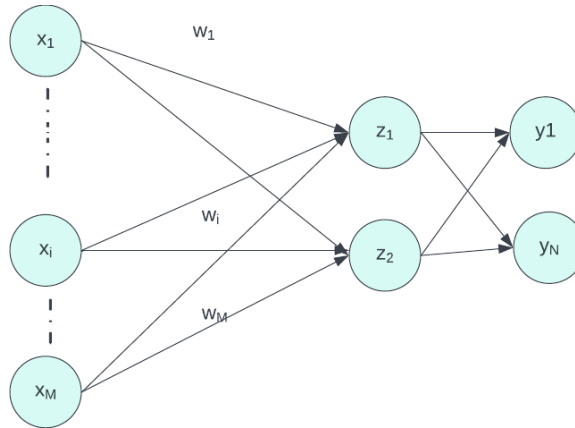


Figure 15: Multilayer perceptron network model.

Neural networks are essentially multilayer perceptron models, where the activation functions are chosen according to the function being approximated by the learning model. The forward propagation of the input X predicts the output Y . The output Z of the hidden layer is given as:

$$Z = \sigma(W_h^T \cdot X) \quad (31)$$

Where σ is the activation function applied to the output of the hidden layer and the subsequent output vector Y is:

$$Y = \sigma_2(W_h^T \cdot Z) \quad (32)$$

Where σ_2 is the activation function applied to the linear combination output of the stage prior to the output stage.

The learning step for a neural network is given by gradient descent minimization and backpropagation of the error computed at the output, to update the weights of the network at each layer in the network, according to the chain rule of differentiation. This process results in a weight update rule which is as follows [141]:

$$Wt \text{ correction} = \frac{\text{learning rate} \times \text{gradient between error of the layer and the weights of the layer}}{\text{input given to the neuron}} \quad (33)$$

Convolutional Neural Network (CNN)

The convolution operation used in Image Processing is typically the cross-correlation of two images. Cross-correlation is a mathematical operation that measures the similarity of two signals as a function of the shift of one signal in relation to the other:

$$f * g = \int_{-\infty}^{\infty} f(\tau)g(t - \tau)d\tau \quad (34)$$

The convolution output $G[x, y]$ of the image $F[x, y]$ and the kernel $h[x, y]$, is given by the discrete cross-correlation of two 2D signals:

$$G[i, j] = \sum_{u=-k}^k \sum_{v=-k}^k h[u, v]F [u + i, v + j] \quad (35)$$

CNNs are particularly performant for the task of pattern recognition in images, videos, and text [138, 139]. These networks are also the backbone of many sophisticated neural network architectures used for the tasks of object detection [140], image segmentation [141], sequence prediction [142], and image generation [143].

Convolutional Neural Networks are an extension of fully connected neural networks. They consist of additional feature extraction layers. The feature extraction layer is comprised of a convolutional layer followed by pooling layers. The convolutional layer convolves multiple filters with the image to extract features of interest called '*feature maps*', rendered useful for the function to be learned by the learning model. An activation function is applied to the outputs of the convolutional operation to introduce non-linearity into the model.

The pooling layer takes the output of the convolutional operation and selects the strongest or the average of all the features computed by the filters. This pooling layer intends to reduce the dimensions of the feature maps. Finally, the output of the convolutional layer is flattened to form a long one-dimensional vector and passed to a fully connected neural network or '*dense layer*' to predict an output based on the feature points extracted by the convolutional layers. The weights of the dense layer and the filters for convolution are the tunable parameters learned by the model during backpropagation and optimized using gradient descent [144].

D. Methodology

I. PMI Data Generation

PMI uses MRT to measure the internally induced temperature increase of the tissue during its irradiation with a NIR laser. MRT provides either 2D or 3D temperature maps. Here, PMI is performed in 2D. Thus, axial MRT slices are used to retrieve the optical properties of the tissue with high resolution and quantitative accuracy. The current PMI setup allows to illuminate the tissue/small animal from four sides, Fig 16. This enables a more significant temperature increase of the tissue compared to the single illumination scheme presented in section B [105]. Achieving higher heating of the tissue allows us to measure MRT maps with better signal-to-noise-ratio, which in turn results in the recovery of higher quality absorption maps.

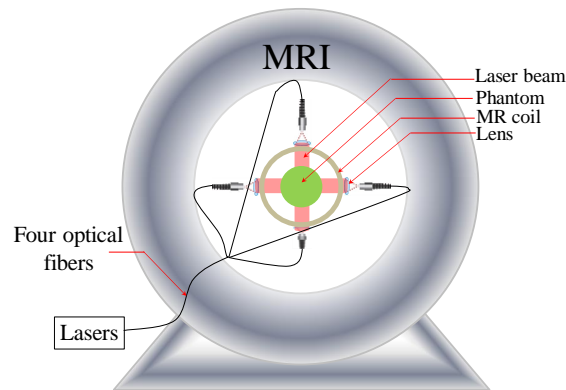


Figure 16: Schematic representation of the PMI instrumentation setup.

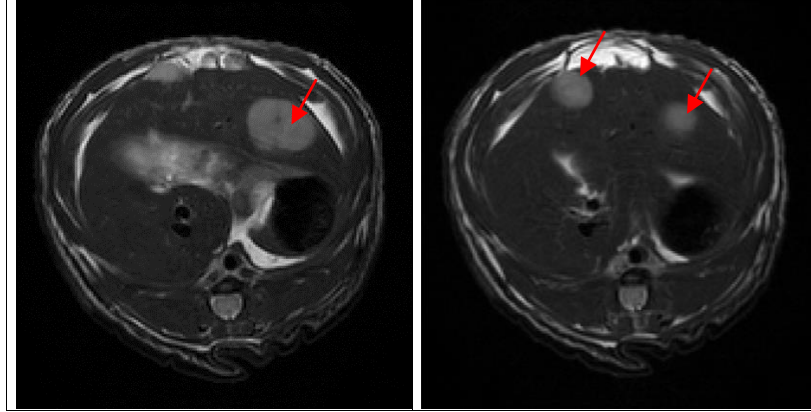


Figure 17: T2-weighted axial slice of a female rat showing the liver bearing: a) single, and b) double tumor as shown by the red arrows

AI approaches require a significant amount of data to perform correctly. In this work, we will generate the necessary data using simulation. Indeed, temperature maps can be obtained by solving the PMI forward problem considering a given geometry having specific optical and thermal properties. Here, the simulated temperature maps are generated using a mice-sized 25 mm diameter cylindrical agar phantom.

The absorption coefficient of the phantom's background is set to model mice muscle tissue, using black India ink to be equal to 0.01 mm^{-1} . The reduced scattering coefficient of the entire phantom is set to be equal to 0.86 mm^{-1} by adjusting the amount of the used intralipids [105]. To mimic the presence of orthotopic tumors, which generally have higher absorption, we inserted inclusions having different sizes and higher absorption coefficients into the phantom. A representative simulated temperature map is presented in Fig 18.

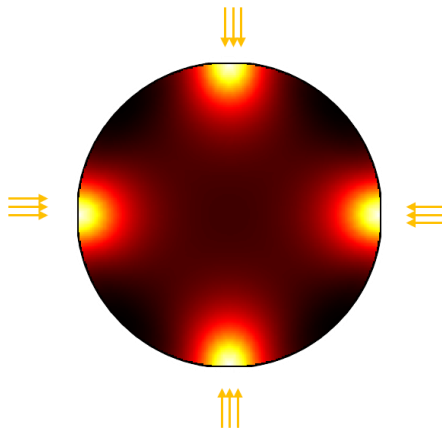


Figure 18: Simulated temperature map obtained by solving the PMI forward problem on a homogeneous phantom ($\mu_a=0.01 \text{ mm}^{-1}$, $\mu_s'=0.86 \text{ mm}^{-1}$), that is heated using four illumination ports.

As can be seen in Fig 18, a significant temperature increase occurs right below the four illumination sites. Then, temperature exponentially decays with depth [102, 114, 115]. When the imaged medium is homogenous, the internal temperature consists of the sum of these four decaying exponential heating functions only. As aforementioned, to mimic the presence of tumors, inclusions with different absorptions are used. In the simulation, the FEM nodes belonging to the used inclusion are selected and their absorption is set to higher values than the background one. Fig 19 depicts examples of different representative inclusions used in our study.

The first row shows a schematic of the cancerous lesions inserted at multiple locations in the phantom. Rows 1-3 show the case using a single node, a single inclusion, and double inclusions with varying radii, respectively. After heating the phantom from its four sides for 8 seconds, the temperature maps obtained are shown in the second row of Fig 19. As for the homogenous phantom in Fig 19, these maps contain the higher temperature increase below the four laser illumination sites. However, additional blobs expressing higher temperature increase are observed deep inside the medium at the location of the inserted inclusions. These higher temperature result from the higher optical absorption of the FEM nodes belonging to that inclusion. These nodes are called '*hot nodes*' in the following sections. To better visualize these hot regions, we subtract the temperature map obtained using the homogeneous phantom in the absence of these inclusions. This resulting difference between the simulated data and the homogenous map is shown in the third row of Fig 19.

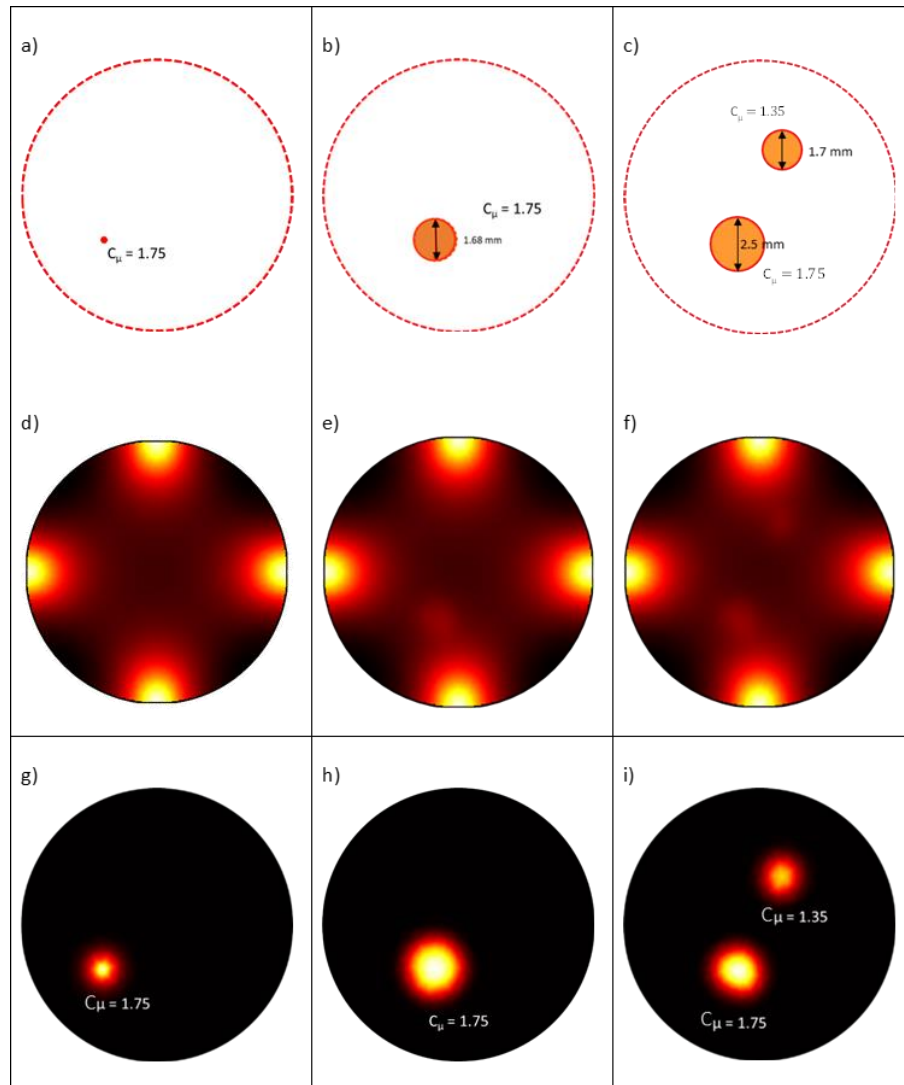


Figure 19: Representative phantoms used to generate the training data. Schematic showing the inclusions containing a) a single node, single inclusion, and c) multiple inclusions. C_{μ} represent the contrast in absorption. d-f) Temperature maps obtained after 8 seconds of heating. g-i) Temperature maps showing the hot blobs at the hot nodes' location after subtraction of the homogeneous temperature map

A dataset of 3927 temperature maps was compiled and carefully studied. These temperature maps were converted to 8-bit maps, thus compelling them to lay within the representational range for an 'unsigned int8' image array.

In Multiwavelength PMI (MW-PMI), the tissue is heated by laser sources of different wavelengths, to obtain the concentrations of different molecules that are characteristic of cancer in the region. These are molecules such as Water, Lipid, Oxygenated Hemoglobin

Deoxygenated Hemoglobin, etc. We can obtain the concentrations of these molecules from the absorption index of the temperature map. To simulate MRT maps corresponding to Multi-Wavelength PMI, we simply variate the absorption indices for the same inclusion. The forward model is run as usual to obtain the MW-PMI maps as shown below. Here we have used a contrast factor C_μ as the ratio of absorption between the background of the phantom and the inclusion in the MRT. Fig 20 b) is an example of a multiple inclusion and multiple absorption temperature map.

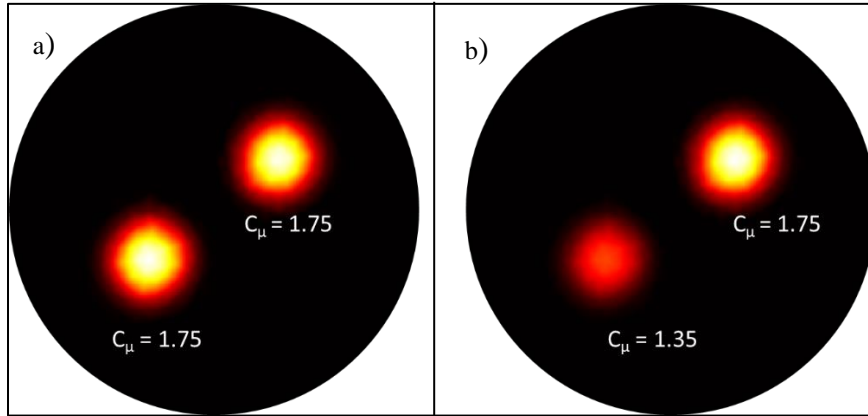


Figure 20: MRT map of a phantom with two inclusions having a) the same contrast factor $C_\mu = 1.75$. b) different contrast factors.

In this thesis, we developed an AI-based algorithm that allows us to detect the hot nodes directly from these difference temperature maps and helps us overcome the limitation caused by temperature diffusion. The recovered information will serve to implement the penalty matrix L used in Eq. 11. The penalty matrix obtained using our new AI-based algorithm will be utilized to guide and constrain the PMI reconstruction algorithm as shown in Eq. 10 to retrieve higher quality images than the ones obtained by the standard algorithm Eq. 8.

II. Direct Detection Using Machine Learning

The problem statement has its roots in pattern recognition. Therefore, it can be framed as a classic ML-based classification problem as follows:

“Given a set of possible outcomes (the total number of nodes N in the FEM mesh), we must classify the data (heat signature from the hot nodes of the MRT map) to fall within a subset of these outcomes. Where all the true outcomes (hot nodes) are labeled 1 and the rest are labeled 0 (the hot-encoded vector)”.

A convolutional neural network (CNN) was therefore decided to be the choice of a machine learning model to be used, typically for its pattern recognition abilities. The output of the forward model gives us a temperature map on a circular phantom as shown in Fig 20. The requirement of any basic image processing algorithm is for the input data to be a matrix. Therefore, the heat map is converted into a minimum enclosing square matrix of size 256x256. We also convert the temperature-driven heat map into a usable 8-bit RGB image. Many processes such as feature extraction, also become less computationally expensive if the data is in a grayscale format.

Therefore, a training pair given to the CNN consisted of a grayscale temperature map at the input side and a hot-encoded labeled vector of length $N \times 1$. We have used two different FEM meshes in this thesis to inspect the robustness of our methodology. We obtained moderate training accuracy but a very low testing accuracy, as the model proceeded to output zero vectors for any image presented to it. Therefore, it was quickly recognized that this classification problem contained two important and hard-to-resolve complications: Class Imbalance and Multiclass Classification.

1. Understanding the class imbalance and multilabel classification

Class imbalance

As seen from the image and the sample mesh diagram in Fig 21 containing the hot nodes, at a given time, there are disproportionately large numbers of nodes that don't belong to the inclusion and are thus labeled zero. We can also view it from an alternate perspective. Assuming a balanced dataset, where each node of the mesh participates roughly equal amounts to the whole dataset, each node across the dataset becomes ‘hot’ only 5% of the time. The model simply does not have enough hot examples of each node to learn from and is hence forced to overfit to all those examples where the node is not contributive or is in an ‘OFF’ state.

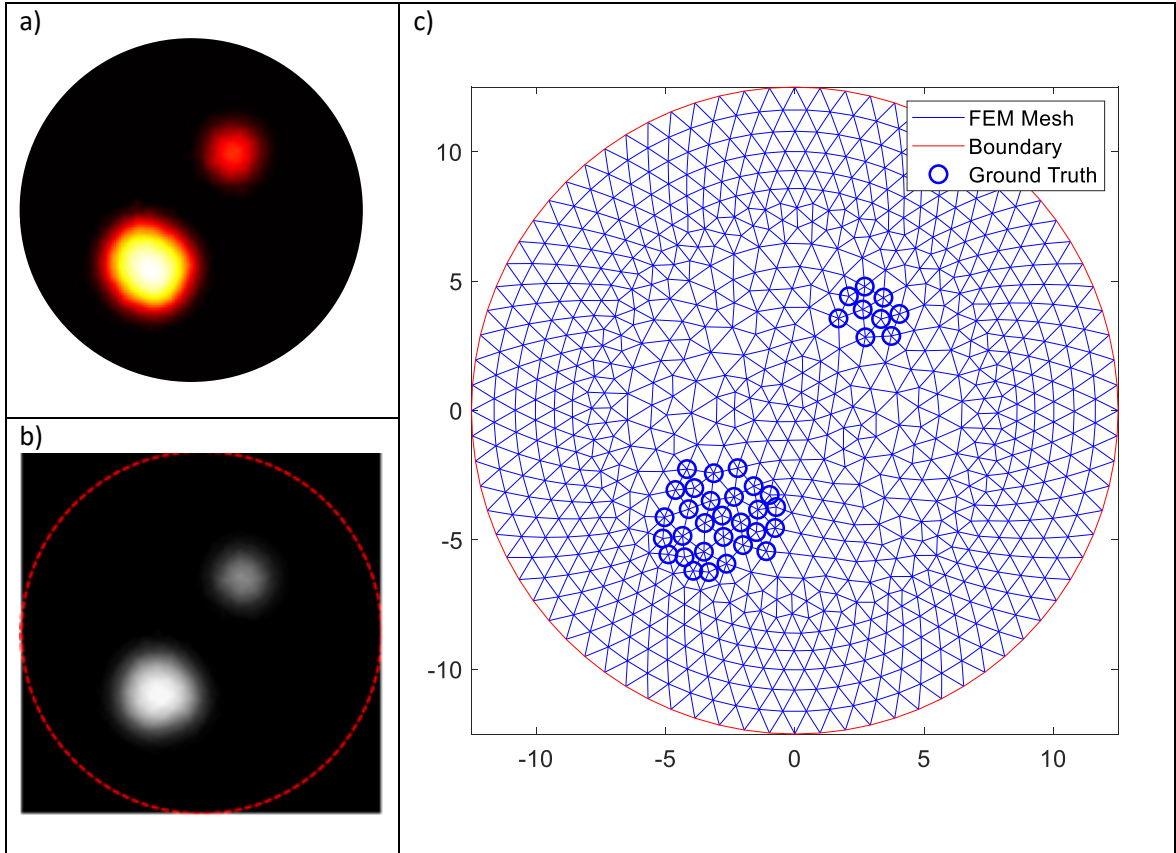


Figure 21: a) temperature map obtained after subtraction of homogeneous map from the simulated MRT containing cancerous inclusions, b) the grayscale MRT map of size 256 x 256, c) FEM mesh showing the hot nodes belonging to the inclusions.

Multilabel classification

In a multiclass classification problem, the output takes more than 2 label values or classes across the dataset. The input in a multiclass classification belongs to only one class out of all possible output classes. Multilabel classification belongs to one of the more challenging classification subtypes where the input falls under multiple classes of outputs at a given time. The possible combinations of classes under which a typical input can fall become huge as the number of classes increase. Since our classification problem has N possible outputs, N being a large value eventually drives this classification problem into almost an unsolvable state.

Resolution for Multilabel classification

It was then resolved to tune the model for multilabel classification using one of the loss functions described in the above section. In particular, weighted loss functions were used in Eq (22), weighing the ‘hot nodes’ by a large factor of 100. We also attempted to use the focal loss given by Eq (24) for training, which focuses on learning the hard-to-learn and sparsely present labels. $\gamma = 11$ was used for the focal loss since the distribution of each label in the data is very low. The model no longer outputted zero vectors but also couldn’t manage to capture the data presented to it. We obtained, albeit nonzero, but very low training accuracies. It was finally decided to decompose the problem into a simpler and more traditional classification problem. It was also decided that the multilabel classification problem will be developed in the future.

III. Region of Interest Localizer and Precision Improver

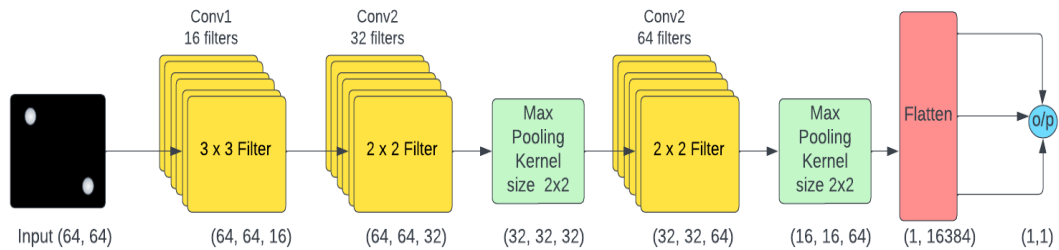


Figure 22: The CNN architecture for ROI identification in a grayscale MRT map.

In this method, we first sought to reduce the total number of possible classes or possible sets of contributory nodes from the complete set of N , to a localized subset. To obtain this localized subset, the following method was executed.

Firstly, the image was split into overlapping square regions and each of these overlapping regions constituted a sub-image. This image splitting was done using kernels of 3 different sizes and shall be called a ‘division kernel’ in this thesis. Each sub-image or region was then assigned a label ‘1’ if the region contained hot nodes, and ‘0’ if it didn’t contain any hot nodes. A CNN model was used for this task of binary classification of sub-images where a training pair for this task consisted of a sub-image and its corresponding label.

Fig 23. shows a typical MRT map containing two inclusions of different sizes and different absorption coefficients, making one highly heated and the other, dimly heated. We understand the importance of division kernel size selection for our task. Here the division kernel is clearly able to capture all of the lower temperature inclusion but only a part of the highly heated inclusion.

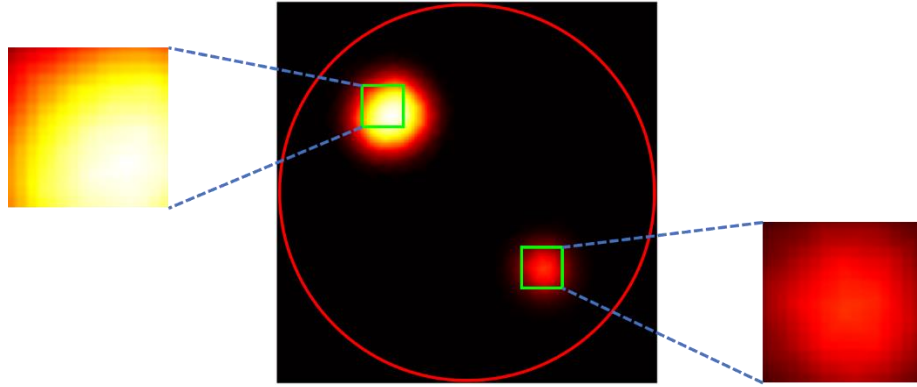


Figure 23: Multi-inclusion MRT with inclusions of different absorption coefficients. Division Kernel size used for region splitting here is 7×7 .

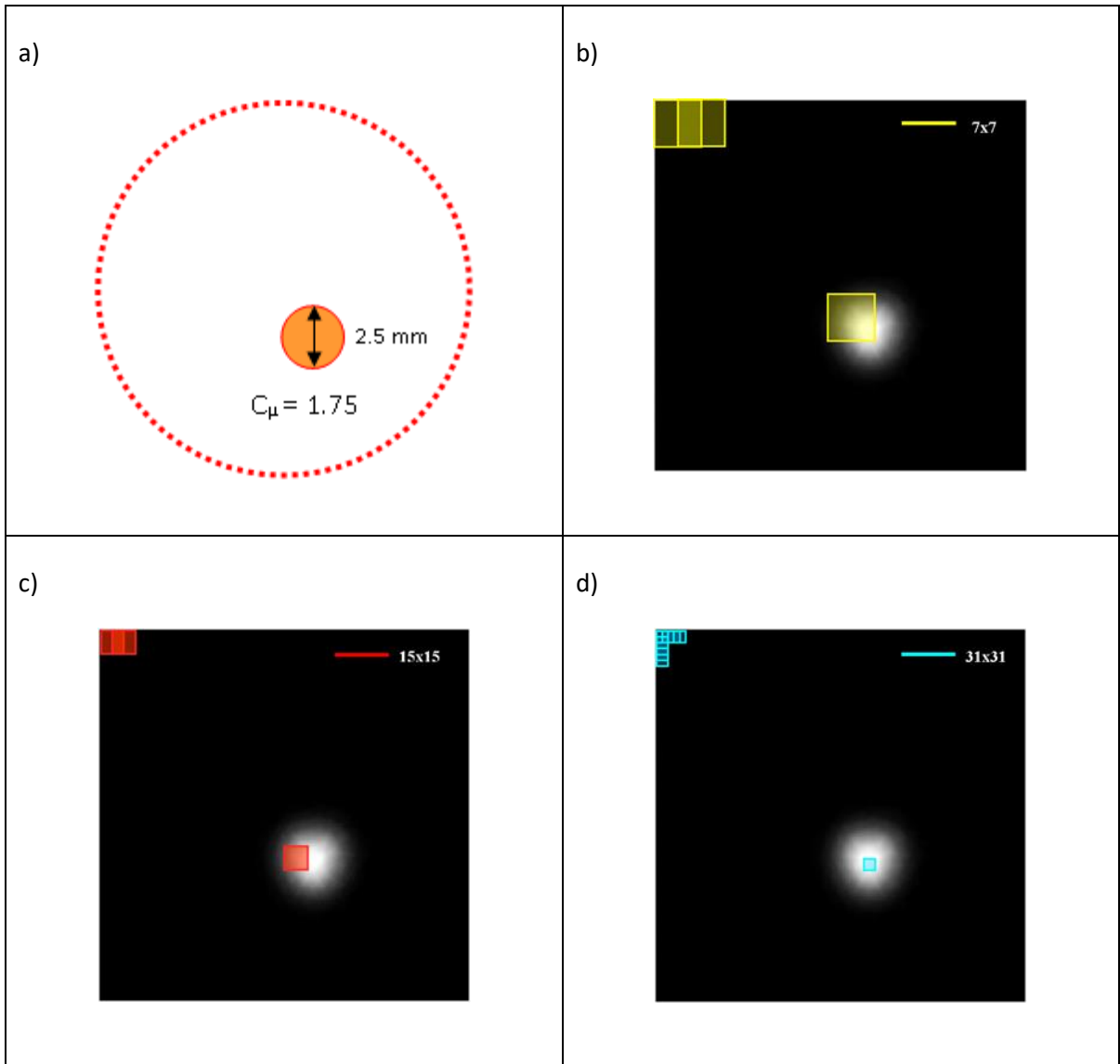


Figure 24: Representative region splitting or division kernels used for ROI prediction, a) Schematic of the used phantom, grayscale temperature map showing division kernels corresponding to: b) 7x7, c) 15x15 and d) 31x31.

This region splitting and classification method neither invoked the class imbalance problem, since the black background can be simply excluded from the training data; nor did it encounter the multi-label classification problem- since this task is comprised of two classes, ‘foreground’, the regions containing the hot nodes, and ‘background’ being the region without any hot nodes.

The machine learning models for each of the region split were trained for a high enough accuracy, where accuracy is declared to be sufficiently ‘high’ for a value greater than 0.9 on both the testing and training datasets. The testing dataset is composed of images never

seen before by the machine learning model. These images are passed through the region of interest localizers to obtain non-zero regions of the image, representing the highest probability of containing an inclusion. The task consists in resolving the regions in temperature maps containing the inclusion of a subset of ‘hot nodes’. For each of the sub-images S_i containing the inclusion, we obtain a set of nodes n_i laying inside the boundaries of the region. We obtain a set of most probable hot nodes H by conducting an intersection over union for the node sets of activated regions.

Howevr, this technique poses a major disadvantage in that it weighs all the nodes laying in an ROI equally. This appears to be incorrect for the cases where a sub-image contains only a small portion of the inclusion, shown in Fig 24.c. This in turn results in a large number of false positives in the estimated output. To resolve this problem, larger divisions of the image, namely 15×15 and 31×31 were constructed but the problem of false positives persisted due to the equal weighting of the nodes in the ROI.

IV. Precision Improvement

After determining a region of interest (ROI), we have to select a subset of probable hot nodes h_i from the set of all the nodes in the region n_i before carrying out the intersection over union over all h_i . This was achieved by using a statistical machine learning model of Regression (15). For a $K \times K$ division of the input image, a total of K^2 Regression Models was used for this task of precision improvement.

The i^{th} sub-image contains a total of n_i possible nodes, comprising the $n_i \times 1$ vector. A value of ‘1’ is assigned to each hot node in the region, and the rest are given the value of ‘0’. If the i^{th} sub-image is an ROI, then the image along with the hot nodes contained within the i^{th} region make up for the training pair of the R_i^{th} learning model.

A training pair for this learning task is composed of a positive sub-image and the hot encoded vector of nodes in the region, then passed to the linear regression model. The linear regression models are trained on the least square minimization technique. The objective of this model is to maximize the R^2 coefficient and reduce the Minimum Mean Square Error values across all training examples. The regression model is said to be optimally trained if the R^2 values for each of the K^2 models are greater than 0.8 since this score would point towards a high level of correlation between the labeled outputs and their corresponding sub-images.

V. The Testing procedure

Once the scores of the Regression models reached the desired value, we proceeded to test the ROI and Precision pipeline by propagating a temperature map through it. The temperature map was first grayscaled, divided into K^2 subdivisions, and passed through the ROI network C_k . For each of the K^2 divisions, an output label was predicted.

The ROI sub-images with positive output labels were pooled and passed to their respective $R^{i^{\text{th}}}$ regression model. A hot vector h_i is predicted for each of the ROI sub-images and an intersection over the union of all those vectors is computed using the linear regression models. The regression model predicts n_i outputs for each i^{th} region. If the value outputted by the regression model is greater than 0.5, then the output is set to '1', or to '0' otherwise. From this hot vector, we obtain a final set of non-zero outputs as the set of hot nodes resulting in the cancerous inclusion. This method exhibited high accuracies for the mesh containing 852 nodes.

VI. Challenges

When the number of nodes of the FEM mesh was increased to 4000 nodes, using a 7×7 division for temperature maps resulted in an average of 81.63 nodes per region. This results in the problem of class imbalance and sparsity in outputs as discussed earlier in this section. Therefore, we have carried region splitting for temperature maps containing 4000 nodes using a 15×15 division kernel. This gives us an average of 17.17 nodes per region to predict for, which we then attempt using classical regression-based multilabel predictions as described above. The methodology showed an average Intersection Over Union (IOU) accuracy of 56% and an accuracy of 82.57% on the intersection with the ground truth. This dip in accuracy has been observed due to the reduction in region size due to an increase in region splitting of the image. We hence need to develop more sophisticated learning models to conduct the multilabel classification for a such fine mesh (4000 nodes).

The ROI-Precision method was trained to work for inclusions of a single absorption level. Therefore, it was imperative to make the above pipeline work for temperature maps across the absorption levels as shown in Fig. 20. This method also failed to predict contributory nodes accurately when the temperature map consisted of multiple inclusions with varying

absorption indices. Hence, it was necessary to add a preprocessing step before the temperature maps were fed into the ROI-Precision pipeline.

VII. Preprocessing for Multi-Absorption Data

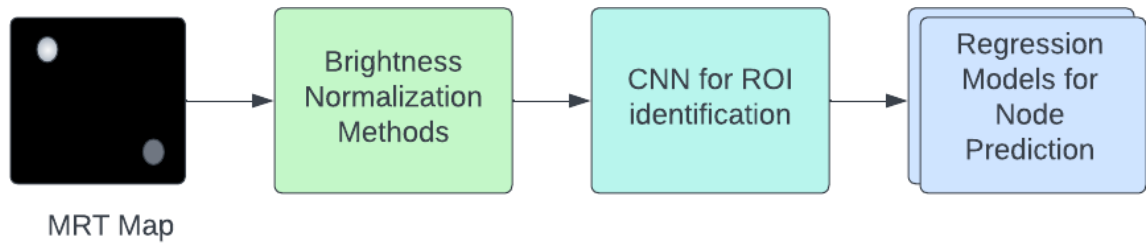


Figure 25: The final methodology developed for hot nodes detection from all MRT maps.

To resolve the problem of the ROI-Precision pipeline adequate for images containing inclusions with different absorption coefficients than the one used to train our pipeline, – i.e, the temperature maps with a contrast factor of value of 1.75, each image was normalized using its maximum. The pipeline was retrained to adapt and fit these normalized pixel values and the accuracies of the resulting CNN and statistical models remained largely unchanged. It is to be noted that all the inclusions in a typical temperature map had the same absorption coefficient.

The temperature maps obtained from the PMI forward model when the contrast factor or the absorption coefficients are changed are temperature maps whose inclusions can have varying gray level ranges. For a high absorption index region, the inclusion will exhibit a higher increase in temperature and therefore a higher gray level. Hence, this stage seeks to process the inclusions so that they fall within the same gray-level range.

1. Image Processing-based Global Pixel Transformations

The task for the preprocessing stage was designed as follows: to increase the pixel intensity values for the inclusion of the lower absorption coefficient (dimmer inclusion) to possess the same peak brightness as the inclusion with a higher absorption coefficient (brighter inclusion). This task was first carried out on a global scale for the image since a local preprocessing technique designed to work separately on the pixels of the bright inclusion and the dimmer inclusion would fail in the case of interacting inclusions. Separability of

the entire inclusions becomes imperative for the reasonable working of the local preprocessing methods such as contour detection and normalization over the pixels in the contour to name a few. Neighborhood-level preprocessing of the image was not adopted to remove the dependency and accuracy of transformations on the neighborhood size. Global level gray level transformations were applied to the image with the constraint that: dim pixels of the inclusion should become brighter while retaining much of their gaussian nature, whereas the bright pixels of the brighter inclusion should remain unchanged. To satisfy these constraints to the maximum possible extent using gray level transformations, the following gray level transformation functions on a typical input image $F(x, y)$ were designed, and the gray level transformed images are denoted by $G(x, y)$.

The resulting images were normalized to be passed through the preprocessing pipeline described above to obtain the set of hot nodes for these MRT images where inclusions with different absorption coefficients are used.

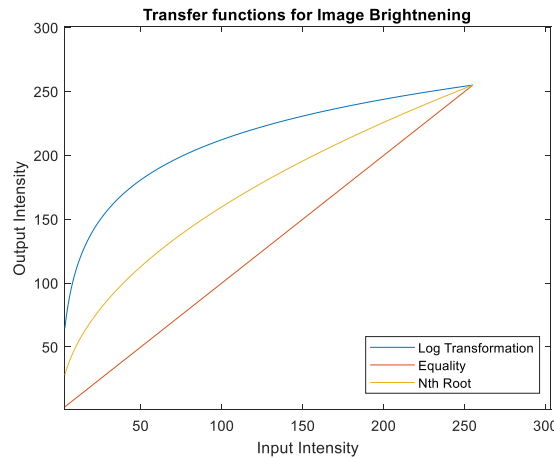


Figure 26: Gray level transformation functions used for image transformation and inclusion normalizing.

2. Drawbacks

A significant drawback in transformations given in Fig 26. is that the entire dim inclusion might lose its gaussian nature as the choice of the function used approaches step-like-behavior. It greatly increases the brightness of the dimmer inclusion but largely maintains its peak brightness. Therefore, the task of normalization of the temperature over its own maximum brightness value did not yield values similar to the values of the MRT for inclusions with equal absorption values.

Hence it was of great importance to retrieve both inclusions separately and normalize them with their respective maximum values to be processed by the ROI-Precision pipeline.

3. Minimum Enclosing Circle detection and Normalization

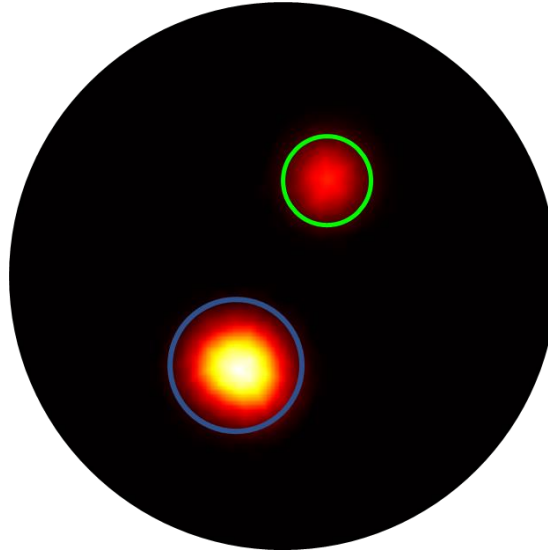


Figure 27: Minimum enclosing circle detection of inclusions in the MRT maps.

To detect the inclusions, the temperature maps are thresholded for all values greater than the tail values of the lowest detectable inclusion. All the features of interest in the image are assigned a gray level of the highest possible gray level considering an unsigned 8-bit integer gray value for each pixel, *i.e.*, 255. The rest are set to 0. We obtain the gradient of the thresholded temperature maps and edge points for objects of interest using the Canny Edge Algorithm [145]. These edge points are used as feature points for the Hough Circle detection algorithm [130] described in the section ??, which allows to obtain the minimum enclosing circles around the inclusions. We have chosen circles as the resolving shape to resolve even the interacting inclusions into separable inclusions, which is not possible to do using algorithms such as contour detection. These circles are drawn on a copy of the original temperature maps. All the pixels inside the circle are normalized with the maximum gray value inside the circular region to be processed by the ROI-precision pipeline for the hot node prediction.

E. Results and Discussion

In this section, we shall first discuss the accuracy scores of the Machine Learning models trained on our dataset produced using the FEM mesh with 852 nodes. The method of the batch training is often used in ML model training. The complete dataset is divided into training and validation sets. A validation set is a set of data on which the model never trained and is used mainly for evaluating the performance of the model during training. These sets are each further decomposed into batches of images. The model learns its parameters by forward propagating through a typical ‘training batch’ and updates its weights by computing the loss on a batch of the validation data. The model is trained in this manner iteratively and each iteration of training and validation or testing is called an ‘epoch’. The objective of the learning model is to maximize its validation accuracy at the end of the training process.

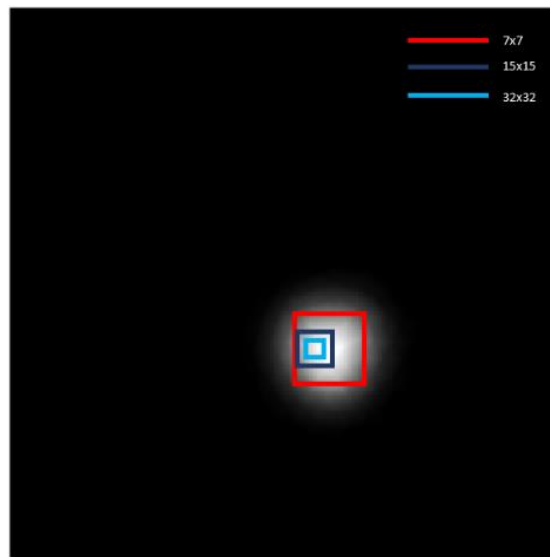


Figure 28: Shows the different region splitting sizes used in our Roi detection network

Division kernel size	Accuracy plots
7x7	<p>Number of Epochs trained</p>
15x15	<p>Number of Epochs trained</p>
31x31	<p>Number of Epochs trained</p>

Table 1: The training and validation accuracies for the CNN ROI prediction model for 7x7, 15x15, and 31x31 division kernels.

I. Representational Diagrams for Results

Single Inclusion

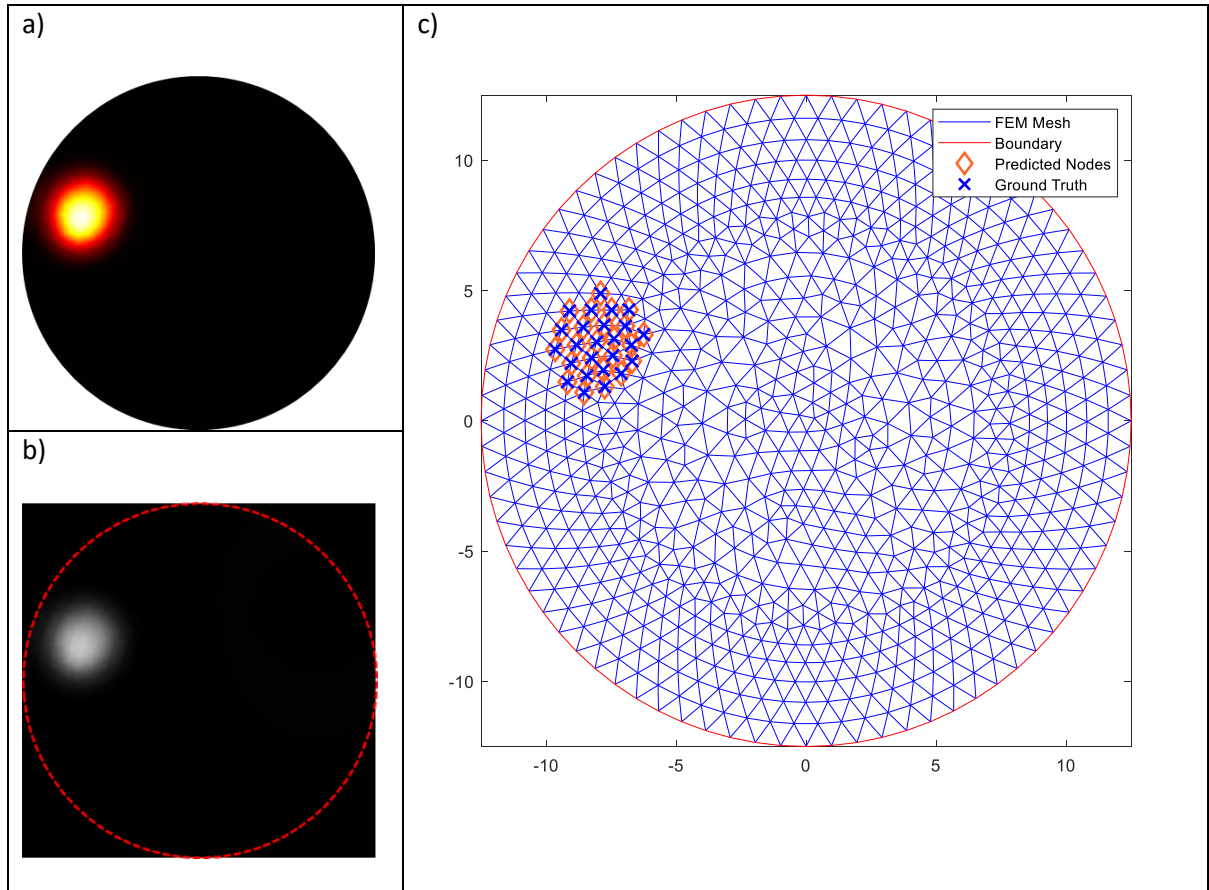


Figure 29: a) MRT map of a single cancerous inclusion of diameter 4 mm and absorption coefficient 0.0165 mm^{-1} , b) the grayscale temperature map, c) Results obtained from the ROI Precision pipeline

The above figure is a representational diagram of the results of a single inclusion temperature map obtained using the ROI-Precision methodology on the schematic of the mesh. Fig 29 a and b are the images of the temperature maps outputted by the forward model and the grayscale operation respectively. 29 c shows the nodes predicted by the method on the schematic of the FEM mesh. It has an overlay of the ground truth predicted nodes, circled in blue, giving us an estimate of the Intersection Over Union Accuracies discussed in this thesis.

Multiple Inclusions

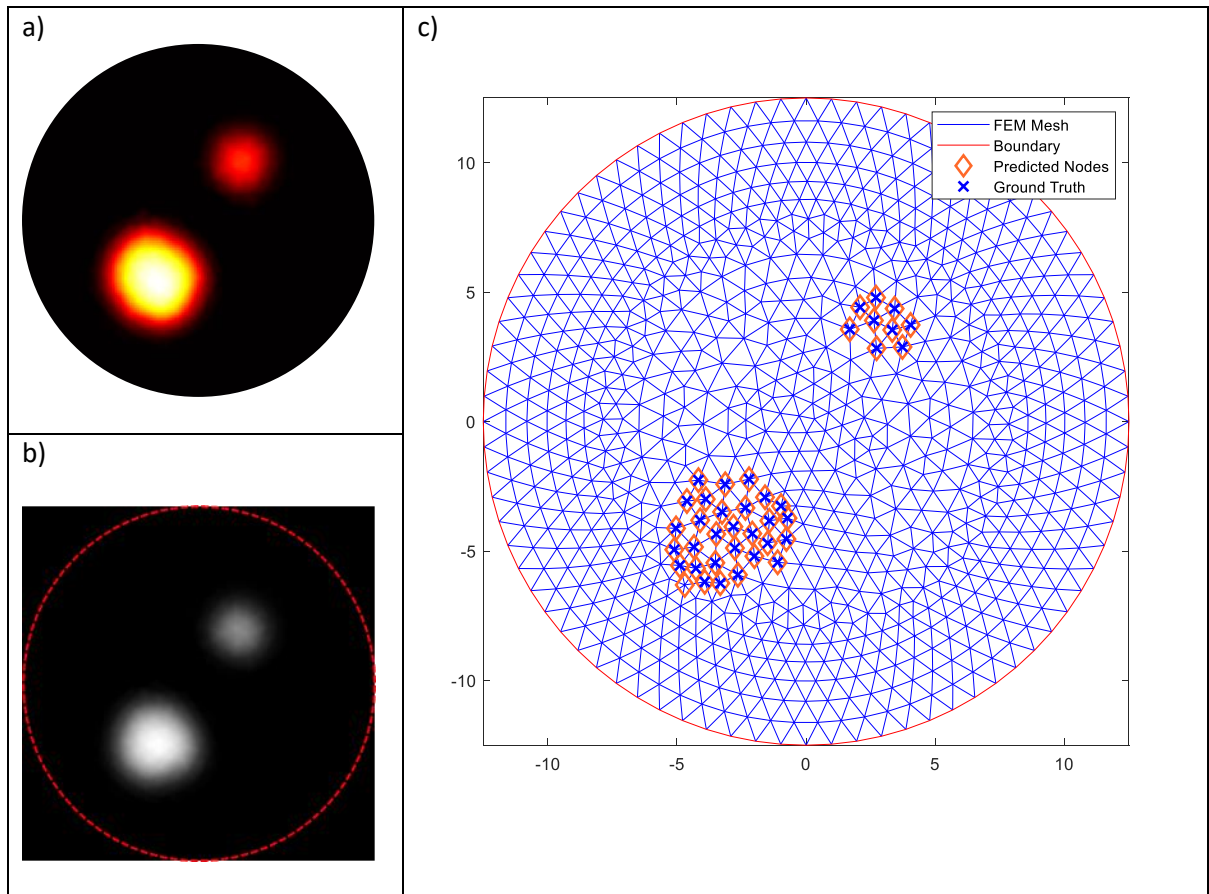


Figure 30: a) the difference temperature map containing two inclusions of different radii 1.75 mm and 1.35 mm and absorption coefficients of 0.017 mm^{-1} and 0.0145 mm^{-1} , respectively. b) grayscale temperature map, c) results obtained using ROI Precision pipeline with Hough Transform.

The above figure is a representational diagram of the results obtained on a multi-absorption and multi inclusion temperature map using the ROI-Precision methodology on the schematic of the mesh. Fig 29 a and b are the images of the temperature maps outputted by the forward model and the grayscale operation respectively. 29 c shows the nodes predicted by the method on the schematic of the FEM mesh. It has an overlay of the ground truth predicted nodes, circled in blue, giving us an estimate of the Intersection Over Union Accuracies discussed in this thesis.

II. Results obtained using the ROI Network

The following table shows the results obtained for apriori reconstruction using the ROI detection as described in the methodology. The accuracy of the network in capturing the highly absorbing nodes of a given inclusion is measured by taking the Intersection Over Union (IOU) score between the predicted labels and the ground truth.

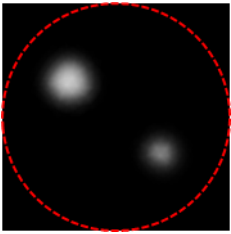
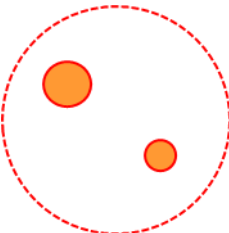
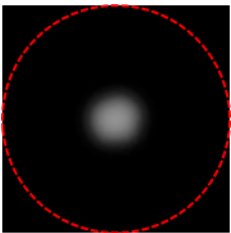
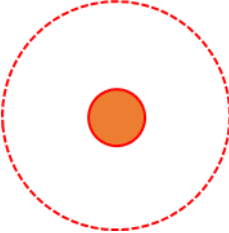
Input Image	Ground Truth	IOU Score (Division Kernel size 7 x 7)	IOU Score (Division Kernel size 15 x 15)	IOU Score (Division Kernel size 31 x 31)
		9.032 %	45.35%	70.70%
		7%	16.15%	31.75%

Table 2: The Intersection Over Union Scores or Overlap scores obtained by using the ROI detection and equal weighing of nodes for the 3 different kernel sizes.

Discussion

We can see from the above-shown prediction results that even the smallest meaningful division (“meaningful” only if the size of the kernel is greater than or equal to the size of a mesh triangle) at its height produces an IOU accuracy of 70.7%. Therefore, this method is neither accurate, consistent nor reliable in predicting the apriori information from the temperature maps. We can also note that there is a large difference in IOU scores for single

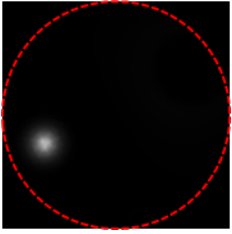
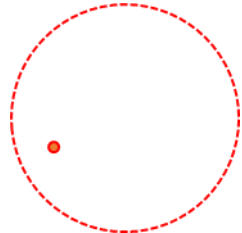
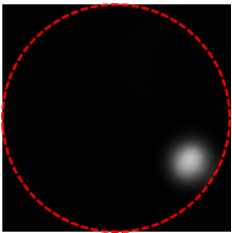
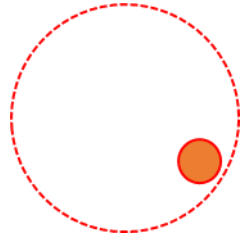
inclusions and multiple inclusions. But it is highly accurate in detecting ROIs as shown in Table 1.

III. Results Obtained using ROI - Precision pipeline

We shall now discuss the results obtained by our ROI - Precision on two broad sets of temperature maps. The following subsections discuss the performance of our methodology on temperature maps containing: a) inclusions of the same absorption coefficients, and b) inclusions of different absorption coefficients. We shall assess the overall performance of the methodology for inclusions as a function of their size, the separation distance between inclusions in the case of double inclusions, and finally as a function of the absorption coefficient of the inclusion.

1. Predictions for a single absorption index

Effect of Size

Temperature map ($\mu_a=0.0165 \text{ mm}^{-1}$)	Ground truth	Diameter of inclusion	IOU score	Accuracy with the ground truth
		1 mm	50%	100%
				TP: 3
				FP: 3
				TN: 846
				FN: 0
		3 mm	100%	100%
				TP: 15
				FP: 0
				TN: 837
				FN: 0

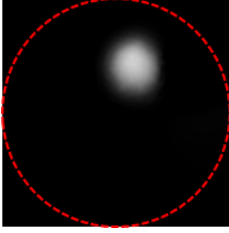
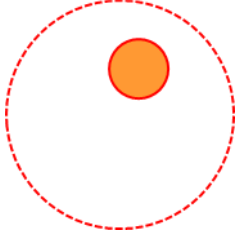
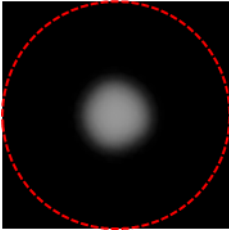
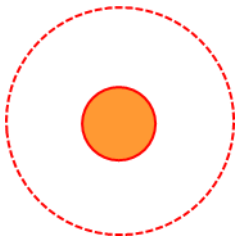
		5 mm	85.29%	100%
				TP: 29
				FP: 5
				TN: 818
				FN: 0
		7 mm	80%	94.11%
				TP: 32
				FP: 8
				TN: 810
				FP: 2

Table 3: ‘Hot node’ prediction accuracy as a function of its size keeping the absorption coefficient constant. The absorption coefficient chosen for this task is 0.0165 mm^{-1} . FP: False Positives, TP: True Positives, TN: True negatives, FN: False Negatives.

Discussion

The above results in Table 3 present the accuracy of the ROI Precision pipeline without the preprocessing using Hough Transformations on temperature maps containing a single inclusion. We measure the accuracy in hot node prediction from the MRT as a function of the size of inclusion. The model tends to overpredict for small-size inclusions, resulting in a low IOU. A low IOU score for small inclusions is mainly due to the small number of hot nodes activated for these regions. It is also to be noted that the model is very precise in its detection of small inclusions, almost averaging a 100% True Positive accuracy.

We can also observe from the above table that the IOU score is near perfect and almost stable for inclusions smaller than 5 mm but greater than 3 mm. The IOU score starts dropping as the size of the inclusion increases. This is mainly because large inclusions activate a large number of ROIs, resulting in an increased possibility of misprediction by the Regression model on each of the ROIs selected by the ROI network.

2. Effect of absorption for Multi-Absorption Inclusions

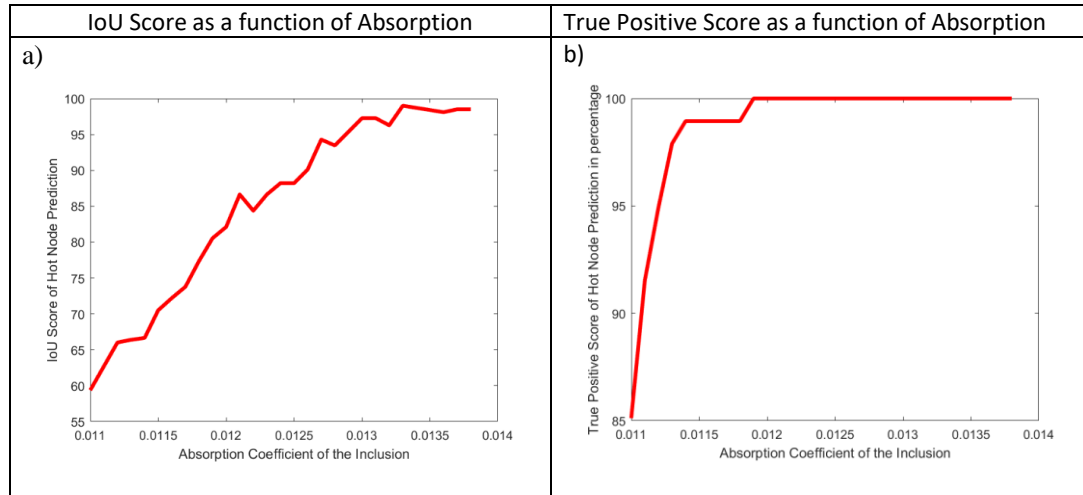


Figure 31: The absorption sensitivity curve a) IOU score as a function of absorption and b) Ground Truth Accuracy as a function of the absorption of Inclusion

Figure 31 shows the IOU scores obtained using a single inclusion phantom. The IOU scores were obtained by gradually varying the absorption coefficient of the inclusion between 0.001 mm^{-1} and 0.014 mm^{-1} , which corresponds to an absorption contrast of 1.1 and 1.4, respectively.

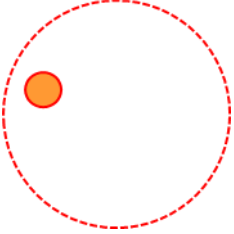
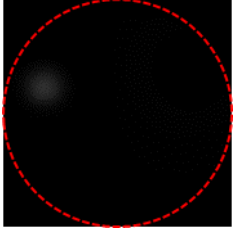
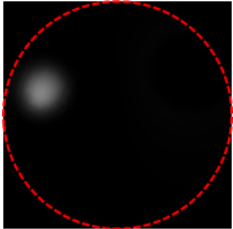
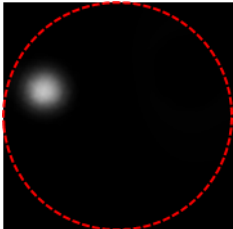
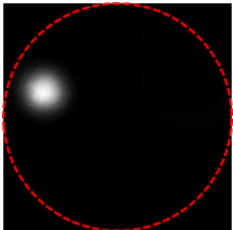
Phantom	Temperature map	Absorption coefficient (mm ⁻¹)	Accuracy with Ground Truth and Confusion Matrix	IOU accuracy (%)
		0.011	100%	73.913
			TP: 17	
			FP: 6	
			TN: 829	
			FN: 0	
		0.0138	92.15%	98.89
			TP: 17	
			FP: 0	
			TN: 835	
			FN: 0	
		0.0165	100%	100
			TP: 17	
			FP: 0	
			TN: 835	
			FN: 0	
		0.0193	100 %	94.44
TP: 17				
FP: 1				
TN: 834				
FN: 0				

Table 4: ‘Hot node’ prediction accuracy as a function of the absorption coefficient of the inclusions. FP: False Positives, TP: True Positives, TN: True negatives, FN: False Negatives.

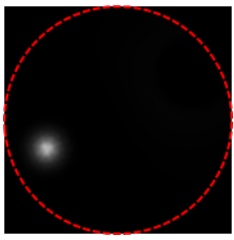
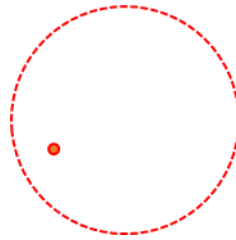
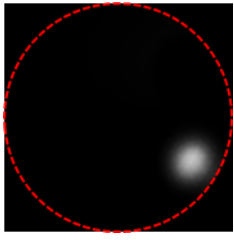
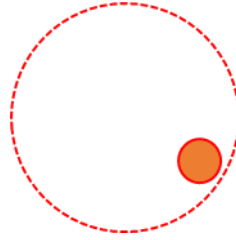
Discussion

The above table describes the accuracies as a function of the absorption coefficient taken of the inclusion. We can see that considering only absorption as a factor, keeping the size and number of inclusions constant, the model tends to overpredict for inclusions of smaller absorption coefficients, resulting in a low IOU score while maintaining a high intersection with the ground truth.

Fig 31. is a sensitivity curve, which measures the IOU score and True positive score of the method as a function of absorption coefficient of the inclusion. From the curve, it can be seen that the model's performance is limited by the absorption coefficient and yields a reasonably high IOU score ($> 85\%$) for an absorption coefficient greater than 0.012mm^{-1} . The model's true positive score remains fairly constant and achieves high values of accuracy for all absorption coefficient values.

3. Effect of Size

We measure the performance of this methodology on MRT maps with inclusions of different sizes using the Mean IOU score and Mean. To ensure independence from absorption, we will test each size with different absorption coefficient values: 0.0120 mm^{-1} , 0.0138 mm^{-1} , 0.0165 mm^{-1} , and 0.019 mm^{-1} .

Temperature map	Ground Truth	Diameter of inclusion	Mean IOU score in percentage	Mean Accuracy with the ground truth
		Single node	50%	100%
		3 mm	100%	100%

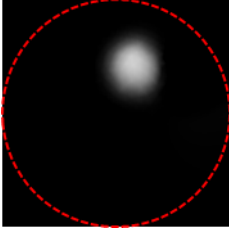
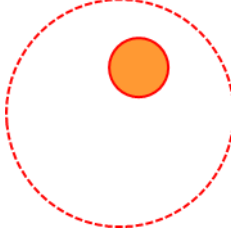
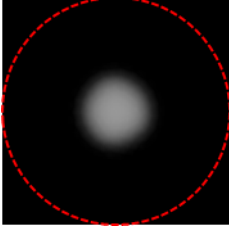
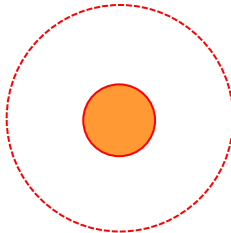
		5 mm	92.2%	100%
		7 mm	89%	97%

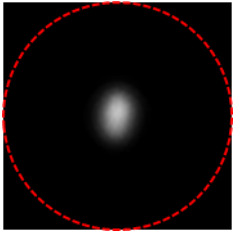
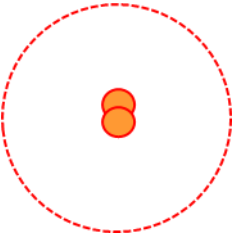
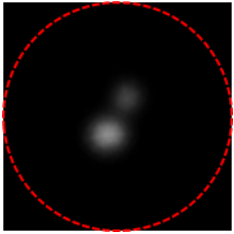
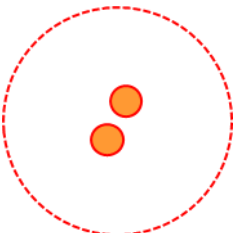
Table 5: ‘Hot node’ prediction accuracy as a function of inclusion size. Each size was tested with variable absorption coefficient values.

Discussion

Table 5 displays the mean accuracies of the methodology as a function of the size of the inclusions. We can infer from these results that the accuracies are not dependent on the position within the phantom. Much similar to our previous results, we obtain low Mean IoU for very small inclusions of the order of a single node and dropping accuracies for very large inclusions of a diameter larger than 6 mm in diameter. The largest inclusion size in our dataset is 7 mm, which correspond to an acceptable maximum tumor size in preclinical studies.

4. Effect of distance between inclusions with different contrasts

Similarly, we measure the performance of this methodology on MRT maps with two inclusions having the same diameter (2.5 mm) using the Mean IOU score and Mean. To ensure independence from absorption, we will test each distance separation with different absorption coefficient values: 0.0120 mm^{-1} , 0.0138 mm^{-1} , 0.0165 mm^{-1} , and 0.019 mm^{-1} .

Temperature maps and corresponding phantoms	Distance between inclusions of diameter 2.5 mm	Mean IOU score in percentage over all absorptions	Mean Accuracy with the ground truth over all absorptions
	0 mm	92.78%	100%
			
	20 mm	50.89%	100.00%
			

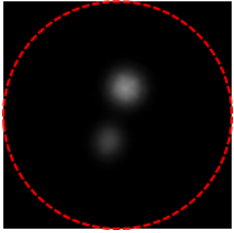
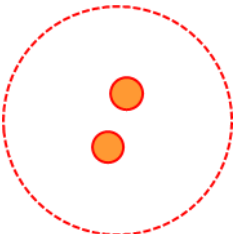
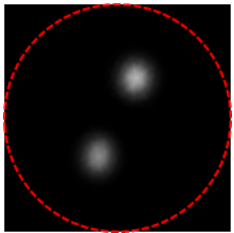
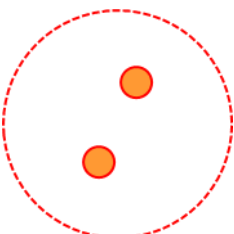
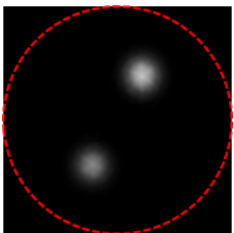
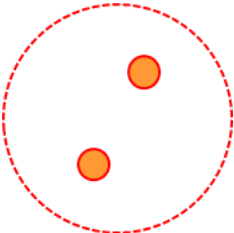
	35 mm	62.55%	92%
			
	65 mm	92.5%	100%
			
	85 mm	82.15%	100%
			

Table 6: Accuracies of the methodology as a function of the distance between the inclusions keeping the diameter of inclusions 2.5 and varying the absorption coefficients.

Discussion

The above-shown results were obtained by varying the separation distance between two inclusions while varying their absorption coefficients and keeping their diameter constant. The chosen constant diameter for this testing was 2.5 mm. We can thus infer that as the inclusions get closer, the mean intersection over union accuracy decreases rapidly and exhibits a rather sharp decline for inclusions that are placed close but are separable. This is due to overprediction by the algorithm after amplifying low-absorption coefficients inclusions. Interacting inclusions display the same mean accuracy as that of a single inclusion.

5. Effect of distance for inclusions with the same absorption coefficient

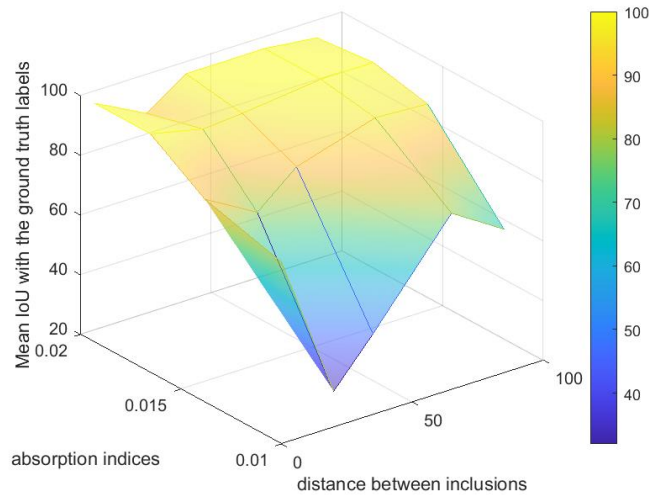


Figure 32: Surface plot showing accuracy as a function of absorption indices or coefficients in the multi-inclusion MRT map and the separation distance between them. The diameter of inclusions was set to 3 mm.

Discussion

The Fig 32. shows us the variation of absorption as a function of the absorption coefficient of the inclusions and the distance between them. Note that the IOU score values typically stay low for low absorption coefficients and for a non-zero small separation distance between the two inclusions as we have seen so far.

F. Conclusion and Future Work

In our research, we have developed a robust pipeline based on machine learning and deep learning techniques in the field of medical imaging. Our research was the first of its kind to be performed at the Center for Functional Onco-Imaging at the University of California, Irvine on Photo Magnetic Imaging Research. It introduced Machine Learning and Deep Learning techniques into the medical imaging research lab. It was also the first study of its kind to use machine learning techniques for apriori reconstruction of inclusions of varying absorptions. We tested our method for the detection of cancerous regions of various sizes, orientations, and absorption coefficients. We evaluated the accuracy of our model prediction as a function of these parameters as well. Our present model is shown to be highly effective for inclusions of sizes greater than 2 mm but less than 7 mm. A sensitivity curve was plotted and studied. It pointed to the usable absorption values of the inclusion for which our method could recover most of the highly absorbing nodes. The model as inferred from the sensitivity curve gives accurate predictions for absorption coefficient values greater than 0.012 mm^{-1} . Furthermore, we discussed the performance of our processing pipeline as a function of a combination of factors such as absorption coefficient and distance separating multiple inclusions in the MRT map. Our methodology also showed high accuracies for temperature maps containing inclusions of high contrast with respect to each other. In addition, our method is really fast since the average time required for the recovery of the hot nodes and building the apriori information from a typical MRT was about 2.75 seconds.

As our methodology shows high apriori prediction accuracies, it holds great promise for improving the quality and efficiency of the PMI reconstruction algorithm. The machine learning-based approach opens new avenues for research in the laboratory to overcome any of the limitations and challenges faced by traditional image processing methods in PMI reconstruction. With continued research and development in machine learning, PMI reconstruction has the potential to revolutionize the diagnosis of a wide range of medical conditions.

To advance the use of machine learning in AI-informed PMI image reconstruction, there are several avenues of research to be explored. When translating our methodology to capture the ‘hot nodes’ on a high-resolution mesh (such as a mesh with 4000 nodes), we observe a rise in the number of regression models being trained in the precision improvement stage from 49 to 225. This stage is computationally expensive and time-consuming. Our future research aims to combine the region of interest prediction network and the regression pipeline into a single highly powerful neural network. This neural

network should be capable of multilabel classification and custom loss functions designed specifically to achieve the objectives of this task.

The future of AI in PMI reconstruction looks very encouraging for students and scholars alike, integrating two of the most rapidly advancing areas of research, Machine Learning and Biomedical Imaging.

References

- [1] A. a. S. I. C. Preda, "Thermal image building inspection for heat loss diagnosis," *Journal of Physics: Conference Series*, vol. 1297, p. 012004, 09 2019, doi: 10.1088/1742-6596/1297/1/012004.
- [2] F. a. P. C. Amon, *Chapter 5 Thermal Imaging in Firefighting and Thermography Applications*. 2010, pp. 279-331.
- [3] E. Goubet, J. Katz, and F. Porikli, *Pedestrian tracking using thermal infrared imaging* (Defense and Security Symposium). SPIE, 2006.
- [4] K. Dolic, A. H. Siddiqui, Y. Karmon, K. Marr, and R. Zivadinov, "The role of noninvasive and invasive diagnostic imaging techniques for detection of extra-cranial venous system anomalies and developmental variants," *BMC Medicine*, vol. 11, no. 1, p. 155, 2013/06/27 2013, doi: 10.1186/1741-7015-11-155.
- [5] M. S. Ozturk, M. G. Montero, L. Wang, L. M. Chaible, M. Jechlinger, and R. Prevedel, "Intravital mesoscopic fluorescence molecular tomography allows non-invasive in vivo monitoring and quantification of breast cancer growth dynamics," *Communications Biology*, vol. 4, no. 1, p. 556, 2021/05/11 2021, doi: 10.1038/s42003-021-02063-8.
- [6] S. N. Histed, M. L. Lindenberg, E. Mena, B. Turkbey, P. L. Choyke, and K. A. Kurdziel, "Review of functional/anatomical imaging in oncology," *Nuclear Medicine Communications*, vol. 33, no. 4, pp. 349-361, 2012, doi: 10.1097/MNM.0b013e32834ec8a5.
- [7] V. Ntziachristos, J. Ripoll, L. V. Wang, and R. Weissleder, "Looking and listening to light: the evolution of whole-body photonic imaging," *Nature biotechnology*, vol. 23, no. 3, pp. 313-320, 2005.
- [8] F. Nouizi, J. Brooks, D. M. Zuro, S. K. Hui, and G. Gulsen, "Implementation of a combined theranostic x-ray irradiator/fluorescence imaging system for automatic assessment of tumor vascular response to radiation therapy," in *Multiscale Imaging and Spectroscopy III, 2022*, vol. 11944: SPIE, pp. 15-19.
- [9] F. Nouizi *et al.*, "Automated in vivo Assessment of Vascular Response to Radiation using a Hybrid Theranostic X-ray Irradiator/Fluorescence Molecular Imaging System," *IEEE Access*, 2020.
- [10] V. Ntziachristos, "Fluorescence molecular imaging," (in eng), *Annu Rev Biomed Eng*, vol. 8, pp. 1-33, 2006, doi: 10.1146/annurev.bioeng.8.061505.095831.
- [11] A. Rudkouskaya, N. Sinsuebphon, J. Ward, K. Tubbesing, X. Intes, and M. Barroso, "Quantitative imaging of receptor-ligand engagement in intact live animals," *Journal of controlled release*, vol. 286, pp. 451-459, 2018.
- [12] M. C. Boonstra *et al.*, "Preclinical evaluation of a novel CEA-targeting near-infrared fluorescent tracer delineating colorectal and pancreatic tumors," *International journal of cancer*, vol. 137, no. 8, pp. 1910-1920, 2015.
- [13] D. Nikkhah, F. Nouizi, R. Hurtado, P. Tabatabaei, and G. Gulsen, "Temperature Modulated Fluorescence Tomography Feasibility Using an Intensified CCD Camera," in *Optics and the Brain, 2022*: Optica Publishing Group, p. JM3A. 9.

- [14] F. Nouizi, H. Erkol, D. Nikkhah, T. C. Kwong, and G. Gulsen, "Development of a preclinical CCD-based temperature modulated fluorescence tomography platform," *Biomedical Optics Express*, vol. 13, no. 11, pp. 5740-5752, 2022.
- [15] F. Nouizi, J. Brooks, D. M. Zuro, S. K. Hui, and G. Gulsen, "Development of a theranostic preclinical fluorescence molecular tomography/cone beam CT-guided irradiator platform," *Biomedical Optics Express*, vol. 13, no. 11, pp. 6100-6112, 2022.
- [16] F. Nouizi, J. Brooks, D. M. Zuro, S. K. Hui, and G. Gulsen, "Theranostic Fluorescence Tomography-Guided Small Animal X-ray Irradiator Platform: System Development and Validation," in *Optical Tomography and Spectroscopy, 2022: Optica Publishing Group*, p. OTu2D. 7.
- [17] F. Nouizi *et al.*, "A thermo-sensitive fluorescent agent based method for excitation light leakage rejection for fluorescence molecular tomography," *Physics in medicine and biology*, 2018.
- [18] T. C. Kwong *et al.*, "Experimental evaluation of the resolution and quantitative accuracy of temperature-modulated fluorescence tomography," *Applied optics*, vol. 56, no. 3, pp. 521-529, 2017.
- [19] T. C. Kwong, F. Nouizi, J. Cho, Y. Lin, U. Sampathkumaran, and G. Gulsen, "Feasibility study of high spatial resolution multimodality fluorescence tomography in ex vivo biological tissue," *Applied optics*, vol. 56, no. 28, pp. 7886-7891, 2017.
- [20] T. C. Kwong, F. Nouizi, U. Sampathkumaran, Y. Zhu, M. M. Alam, and G. Gulsen, "Activatable thermo-sensitive ICG encapsulated pluronic nanocapsules for temperature sensitive fluorescence tomography," in *SPIE BiOS, 2015: International Society for Optics and Photonics*, pp. 93390C-93390C-6.
- [21] Y. Lin, F. Nouizi, T. C. Kwong, and G. Gulsen, "Simulation-based evaluation of the resolution and quantitative accuracy of temperature-modulated fluorescence tomography," (in eng), *Appl Opt*, vol. 54, no. 25, pp. 7612-21, Sep 2015.
- [22] F. Nouizi *et al.*, "Excitation light leakage suppression using temperature sensitive fluorescent agents," in *SPIE BiOS, 2015: International Society for Optics and Photonics*, pp. 93190Y-93190Y-5.
- [23] F. Nouizi, T. C. Kwong, J. Cho, Y. Lin, U. Sampathkumaran, and G. Gulsen, "Implementation of a new scanning method for high-resolution fluorescence tomography using thermo-sensitive fluorescent agents," (in eng), *Opt Lett*, vol. 40, no. 21, pp. 4991-4, Nov 2015.
- [24] J. Zheng, F. Nouizi, F. Cho, J. Kwong, and G. Gulsen, "High resolution 3D fluorescence tomography using ballistic photons," in *SPIE BiOS, 2015: International Society for Optics and Photonics*, pp. 93191V-93191V-5.
- [25] J. Kwong, F. Nouizi, Y. Li, J. Chen, M. Su, and G. Gulsen, "Simulation of optical breast density measurements using structured light illumination," in *SPIE BiOS, 2014: International Society for Optics and Photonics*, pp. 893717-893717-8.
- [26] T. C. Kwong *et al.*, "Validation of temperature-modulated fluorescence tomography in vivo," in *SPIE BiOS, 2014: International Society for Optics and Photonics*, pp. 89370H-89370H-7.
- [27] T. C. Kwong, F. Nouizi, Y. Lin, Y. Sampathkumaran, A. Shaaz, and G. Gulsen, "Temperature-modulated fluorescence tomography: modulating tissue temperature

- using HIFU for high-resolution in vivo fluorescence tomography," in *SPIE BiOS*, 2013, pp. 857405-857405-8
- [28] F. Nouizi, "Preclinical, fluorescence and diffuse optical tomography: non-contact instrumentation, modeling and time-resolved 3D reconstruction," France, 2011.
- [29] F. Gao *et al.*, "A fiber-based, non-contact scheme for time-domain diffuse fluorescence tomography: methodology and simulative validation," in *SPIE BiOS*, 2010: International Society for Optics and Photonics, pp. 755700-755700-9.
- [30] F. Nouizi, R. Chabrier, M. Torregrossa, and P. Poulet, "3D modeling for solving forward model of no-contact Fluorescence Diffuse Optical Tomography method," in *European Conferences on Biomedical Optics*, Munich, Germany, 2009: International Society for Optics and Photonics, pp. 73690C-73690C-10.
- [31] P.-A. Lo, J. Cho, F. Nouizi, H. K. Chiang, and G. Gulsen, "Multispectral fluorescence diffuse optical tomography," in *Design and Quality for Biomedical Technologies X*, 2017, vol. 10056: SPIE, pp. 172-176.
- [32] D. Faulkner, M. Ochoa, N. I. Nizam, S. Gao, and X. Intes, "Diffuse Fluorescence Tomography," in *Biomedical Optical Imaging: From Nanoscopy to Tomography*: AIP Publishing LLC Melville, New York, 2021, pp. 11-1-11-28.
- [33] L. Hardy, D. Sforza, I. Iordachita, X. Xu, J. W. Wong, and K. K.-H. Wang, "Development of a mobile fluorescence tomography-guided system for pre-clinical radiotherapy research," in *Optical Tomography and Spectroscopy*, 2020: Optical Society of America, p. SW1D. 6.
- [34] J. A. Benitez, C. Zanca, J. Ma, W. K. Cavenee, and F. B. Furnari, "Fluorescence Molecular Tomography for In Vivo Imaging of Glioblastoma Xenografts," (in eng), *J Vis Exp*, no. 134, 04 2018, doi: 10.3791/57448.
- [35] Y. Zhang, L. Zhang, G. Yin, W. Ma, and F. Gao, "Assessing indocyanine green pharmacokinetics in mouse liver with a dynamic diffuse fluorescence tomography system," *Journal of Biophotonics*, p. e201800041, 2018.
- [36] X. Ma *et al.*, "Integrin-Targeted Hybrid Fluorescence Molecular Tomography/X-ray Computed Tomography for Imaging Tumor Progression and Early Response in Non-Small Cell Lung Cancer," *Neoplasia*, vol. 19, no. 1, pp. 8-16, 2017.
- [37] J. Shi, T. S. Udayakumar, Z. Wang, N. Dogan, A. Pollack, and Y. Yang, "Optical molecular imaging-guided radiation therapy part 2: Integrated x-ray and fluorescence molecular tomography," *Medical physics*, vol. 44, no. 9, pp. 4795-4803, 2017.
- [38] Q. Pian, R. Yao, L. Zhao, and X. Intes, "Hyperspectral time-resolved wide-field fluorescence molecular tomography based on structured light and single-pixel detection," (in eng), *Opt Lett*, vol. 40, no. 3, pp. 431-4, Feb 2015.
- [39] J. Cho, S. W. Jeon, J. Zheng, C.-S. Kim, O. Nalcioglu, and G. Gulsen, "Development of a spectrally-resolved fluorescence tomography system using a NIR swept laser and a digital micromirror array based detection system," in *SPIE BiOS*, 2014: International Society for Optics and Photonics, pp. 89470Z-89470Z-6.
- [40] C. Darne, Y. Lu, and E. M. Sevick-Muraca, "Small animal fluorescence and bioluminescence tomography: a review of approaches, algorithms and technology update," *Physics in medicine and biology*, vol. 59, no. 1, p. R1, 2014.

- [41] C. Darne, Y. Lu, and E. M. Sevick-Muraca, "Small animal fluorescence and bioluminescence tomography: a review of approaches, algorithms and technology update," *Physics in Medicine & Biology*, vol. 59, no. 1, p. R1, 2013.
- [42] A. Ale, V. Ermolayev, E. Herzog, C. Cohrs, M. H. de Angelis, and V. Ntziachristos, "FMT-XCT: in vivo animal studies with hybrid fluorescence molecular tomography-X-ray computed tomography," (in Eng), *Nat Methods*, May 6 2012, doi: 10.1038/nmeth.2014.
- [43] J. McGinty *et al.*, "In vivo fluorescence lifetime tomography of a FRET probe expressed in mouse," (in eng), *Biomed Opt Express*, vol. 2, no. 7, pp. 1907-17, Jul 1 2011, doi: 10.1364/boe.2.001907.
- [44] K. M. Tichauer *et al.*, "Imaging workflow and calibration for CT-guided time-domain fluorescence tomography," (in eng), *Biomed Opt Express*, vol. 2, no. 11, pp. 3021-36, Nov 1 2011, doi: 10.1364/boe.2.003021.
- [45] W. C. Barber, Y. Lin, O. Nalcioglu, J. S. Iwanczyk, N. E. Hartsough, and G. Gulsen, "Combined fluorescence and X-Ray tomography for quantitative in vivo detection of fluorophore," (in eng), *Technol Cancer Res Treat*, Research Support, N.I.H., Extramural vol. 9, no. 1, pp. 45-52, Feb 2010.
- [46] Y. Lin *et al.*, "Quantitative fluorescence tomography using a combined tri-modality FT/DOT/XCT system," *Optics Express*, vol. 18, no. 8, pp. 7835-7850, 2010.
- [47] J. Goonawardena, C. Yong, and M. Law, "Use of indocyanine green fluorescence compared to radioisotope for sentinel lymph node biopsy in early-stage breast cancer: systematic review and meta-analysis," *The American Journal of Surgery*, 2020.
- [48] Z. Hu *et al.*, "First-in-human liver-tumour surgery guided by multispectral fluorescence imaging in the visible and near-infrared-I/II windows," *Nature biomedical engineering*, vol. 4, no. 3, pp. 259-271, 2020.
- [49] Y. Ardeshirpour, D. L. Sackett, J. R. Knutson, and A. H. Gandjbakhche, "Using in vivo fluorescence lifetime imaging to detect HER2-positive tumors," *EJNMMI research*, vol. 8, no. 1, p. 26, 2018.
- [50] H. Xiong *et al.*, "High-Contrast Fluorescence Detection of Metastatic Breast Cancer Including Bone and Liver Micrometastases via Size-Controlled pH-Activatable Water-Soluble Probes," (in eng), *Adv Mater*, vol. 29, no. 29, Aug 2017, doi: 10.1002/adma.201700131.
- [51] T. H. Degett, H. S. Andersen, and I. Gögenur, "Indocyanine green fluorescence angiography for intraoperative assessment of gastrointestinal anastomotic perfusion: a systematic review of clinical trials," *Langenbeck's archives of surgery*, vol. 401, no. 6, pp. 767-775, 2016.
- [52] A. V. DSouza, H. Lin, E. R. Henderson, K. S. Samkoe, and B. W. Pogue, "Review of fluorescence guided surgery systems: identification of key performance capabilities beyond indocyanine green imaging," *Journal of biomedical optics*, vol. 21, no. 8, p. 080901, 2016.
- [53] J. Seo *et al.*, "Principal component analysis of dynamic fluorescence images for diagnosis of diabetic vasculopathy," *Journal of biomedical optics*, vol. 21, no. 4, p. 046003, 2016.
- [54] F. D. Dip, T. Ishizawa, N. Kokudo, and R. J. Rosenthal, "Fluorescence Imaging for Surgeons," 2015.

- [55] B. D. H. M. E. L. D. C. A. K. M. G. R. J. Boas D A and Q. Zhang, "Imaging the body with diffuse optical tomography," *IEEE Sig. Proc. Mag.*, vol. 18, no. 6, p. 57, 2001.
- [56] Y. Hoshi and Y. Yamada, "Overview of diffuse optical tomography and its clinical applications," *Journal of biomedical optics*, vol. 21, no. 9, pp. 091312-091312, 2016.
- [57] L. Kocsis, P. Herman, and A. Eke, "The modified Beer-Lambert law revisited," (in ENG), *Phys Med Biol*, vol. 51, no. 5, pp. N91-8, Mar 2006, doi: 10.1088/0031-9155/51/5/N02.
- [58] F. Nouizi, GilbertoDiaz-Ayil, F. XavierBlé, BenoitDubois, WilfriedUhring, and P. Poulet, "Time-gated near-infrared spectroscopic imaging of brain activation: a simulation proof of concept," in *SPIE BiOS, San Francisco, 2011*, vol. 7896: SPIE, Optical Tomography and Spectroscopy of Tissue IX, ed., pp. 78960L-78960L.
- [59] F. Nouizi, M. Torregrossa, O. Geneveaux, R. Chabrier, and P. Poulet, "3D modeling of noncontact fiber-based approach for time-resolved diffuse optical tomography," in *Optical Tomography and Spectroscopy of Tissue IX*, 2011, vol. 7896: International Society for Optics and Photonics, p. 78961Z.
- [60] F. Nouizi, M. Torregrossa, R. Chabrier, and P. Poulet, "Improvement of absorption and scattering discrimination by selection of sensitive points on temporal profile in diffuse optical tomography," (in eng), *Opt Express*, vol. 19, no. 13, pp. 12843-54, Jun 2011.
- [61] F. Nouizi, G. Diaz-Ayil, F.-X. Blé, B. Dubois, W. Uhring, and P. Poulet, "Time-gated near-infrared spectroscopic imaging of brain activation: a simulation proof of concept," in *SPIE BIOS, San Francisco, SPIE, Ed., 2011*, vol. 7896: International Society for Optics and Photonics, pp. 78960L-78960L-8.
- [62] M. Amouroux *et al.*, "L'imagerie spectroscopique proche infrarouge," presented at the Colloque Imagerie pour les Sciences du Vivant et de la Médecine, Mulhouse, France, 2009.
- [63] H. Dehghani *et al.*, "Near infrared optical tomography using NIRFAST: Algorithm for numerical model and image reconstruction," *Communications in numerical methods in engineering*, vol. 25, no. 6, pp. 711-732, 2009.
- [64] H. Dehghani, S. Srinivasan, B. W. Pogue, and A. Gibson, "Numerical modelling and image reconstruction in diffuse optical tomography," (in eng), *Philos Trans A Math Phys Eng Sci*, vol. 367, no. 1900, pp. 3073-93, Aug 2009, doi: 10.1098/rsta.2009.0090.
- [65] A. Gibson and H. Dehghani, "Diffuse optical imaging," (in eng), *Philos Trans A Math Phys Eng Sci*, vol. 367, no. 1900, pp. 3055-72, Aug 2009, doi: 10.1098/rsta.2009.0080.
- [66] S. Arridge, "Optical tomography in medical imaging," (in English), *Inverse Problems*, Review vol. 15, no. 2, pp. R41-R93, APR 1999 1999, doi: 10.1088/0266-5611/15/2/022.
- [67] H. Erkol, F. Nouizi, M. B. Unlu, and G. Gulsen, "An extended analytical approach for diffuse optical imaging," *Physics in medicine and biology*, vol. 60, no. 13, p. 5103, 2015.
- [68] M. Guven, B. Yazici, X. Intes, and B. Chance, "Diffuse optical tomography with a priori anatomical information," (in eng), *Phys Med Biol*, Research Support, N.I.H.,

- Extramural Research Support, U.S. Gov't, Non-P.H.S. Research Support, U.S. Gov't, P.H.S. vol. 50, no. 12, pp. 2837-58, Jun 21 2005, doi: 10.1088/0031-9155/50/12/008.
- [69] X. Intes, C. Maloux, M. Guven, B. Yazici, and B. Chance, "Diffuse optical tomography with physiological and spatial a priori constraints," *Phys Med Biol*, vol. 49, no. 12, pp. N155-63, Jun 21 2004.
- [70] X. Intes, V. Ntziachristos, J. P. Culver, A. Yodh, and B. Chance, "Projection access order in algebraic reconstruction technique for diffuse optical tomography," *Phys Med Biol*, vol. 47, no. 1, pp. N1-10, Jan 7 2002.
- [71] A. T. Eggebrecht *et al.*, "Mapping distributed brain function and networks with diffuse optical tomography," (in ENG), *Nat Photonics*, vol. 8, no. 6, pp. 448-454, Jun 2014, doi: 10.1038/nphoton.2014.107.
- [72] Y. Yamada and S. Okawa, "Diffuse optical tomography: Present status and its future," *Optical Review*, vol. 21, no. 3, pp. 185-205, 2014.
- [73] J. Cho, Y. Lin, G. Gulsen, O. Nalcioglu, M. Y. Jeong, and C.-S. Kim, "Development of near-infrared swept laser based diffuse optical tomography system," in *Biomedical Optics, 2012: Optical Society of America*, p. BW1A. 3.
- [74] D. T. Y Lin, O Nalcioglu and G Gulsen,, "Tumor Characterization in Small Animals Using MR-guided Dynamic Contrast Enhanced Diffuse Optical Tomography (DCE-DOT)," *Journal of Biomedical Optics*, vol. In press, 2011.
- [75] B. J. Tromberg, B. W. Pogue, K. D. Paulsen, A. G. Yodh, D. A. Boas, and A. E. Cerussi, "Assessing the future of diffuse optical imaging technologies for breast cancer management," (in eng), *Med Phys*, Research Support, N.I.H., Extramural vol. 35, no. 6, pp. 2443-51, Jun 2008.
- [76] Z. Yuan, Q. Zhang, E. S. Sobel, and H. Jiang, "Tomographic x-ray-guided three-dimensional diffuse optical tomography of osteoarthritis in the finger joints," *J Biomed Opt*, vol. 13, no. 4, p. 044006, Jul-Aug 2008.
- [77] G. M. Hale and M. R. Querry, "Optical constants of water in the 200-nm to 200- μ m wavelength region," *Applied optics*, vol. 12, no. 3, pp. 555-563, 1973.
- [78] R. L. van Veen, H. J. Sterenborg, A. Pifferi, A. Torricelli, E. Chikoidze, and R. Cubeddu, "Determination of visible near-IR absorption coefficients of mammalian fat using time- and spatially resolved diffuse reflectance and transmission spectroscopy," *J Biomed Opt*, vol. 10, no. 5, p. 054004, Sep-Oct 2005.
- [79] J. Ruiz *et al.*, "Breast density quantification using structured-light-based diffuse optical tomography simulations," *Applied optics*, vol. 56, no. 25, pp. 7146-7157, 2017.
- [80] A. Corlu *et al.*, "Diffuse optical tomography with spectral constraints and wavelength optimization," *Appl Opt*, vol. 44, no. 11, pp. 2082-93, Apr 10 2005.
- [81] A. Li, Q. Zhang, J. P. Culver, E. L. Miller, and D. A. Boas, "Reconstructing chromosphere concentration images directly by continuous-wave diffuse optical tomography," *Opt Lett*, vol. 29, no. 3, pp. 256-8, Feb 1 2004.
- [82] M. L. Altoe *et al.*, "Diffuse optical tomography of the breast: a potential modifiable biomarker of breast cancer risk with neoadjuvant chemotherapy," *Biomedical optics express*, vol. 10, no. 8, pp. 4305-4315, 2019.

- [83] H. Vavadi *et al.*, "Compact ultrasound-guided diffuse optical tomography system for breast cancer imaging," *Journal of biomedical optics*, vol. 24, no. 2, p. 021203, 2018.
- [84] H. Ban *et al.*, "Heterodyne frequency-domain multispectral diffuse optical tomography of breast cancer in the parallel-plane transmission geometry," *Medical Physics*, vol. 43, no. 7, pp. 4383-4395, 2016.
- [85] G. Quarto, A. Torricelli, L. Spinelli, A. Pifferi, R. Cubeddu, and P. Taroni, "Breast Monitoring by Time-Resolved Diffuse Optical Imaging," in *Advanced Time-Correlated Single Photon Counting Applications*: Springer, 2015, pp. 587-611.
- [86] M. R. Hajihashemi, S. R. Grobmyer, S. Z. Al-Quran, and H. Jiang, "Noninvasive evaluation of nuclear morphometry in breast lesions using multispectral diffuse optical tomography," (in eng), *PLoS One*, Case Reports Research Support, N.I.H., Extramural Research Support, Non-U.S. Gov't vol. 7, no. 9, p. e45714, 2012, doi: 10.1371/journal.pone.0045714.
- [87] S. R. Arridge and M. Schweiger, "Image reconstruction in optical tomography," *Philos Trans R Soc Lond B Biol Sci*, vol. 352, no. 1354, pp. 717-26, Jun 29 1997.
- [88] S. R. Arridge and J. C. Hebden, "Optical imaging in medicine: II. Modelling and reconstruction," *Phys Med Biol*, vol. 42, no. 5, pp. 841-53, May 1997.
- [89] A. S. R. Hebden J C and D. T. Delpy, "Optical imaging in medicine: I. Experimental techniques," *Phys. Med. Biol.*, vol. 42, no. 5, p. 825, 1997.
- [90] B. Meng *et al.*, "Noninvasive imaging of dual-agent uptake in glioma and normal tissue using MRI-coupled fluorescence tomography," in *Optical Tomography and Spectroscopy of Tissue XIII*, 2019, vol. 10874: International Society for Optics and Photonics, p. 1087413.
- [91] S. C. Davis *et al.*, "Dynamic dual-tracer MRI-guided fluorescence tomography to quantify receptor density in vivo," *Proceedings of the National Academy of Sciences*, vol. 110, no. 22, pp. 9025-9030, 2013.
- [92] S. C. Davis *et al.*, "MRI-coupled fluorescence tomography quantifies EGFR activity in brain tumors," (in eng), *Acad Radiol*, vol. 17, no. 3, pp. 271-6, Mar 2010, doi: 10.1016/j.acra.2009.11.001.
- [93] F. Leblond, S. C. Davis, P. A. Valdes, and B. W. Pogue, "Pre-clinical whole-body fluorescence imaging: Review of instruments, methods and applications," *J Photochem Photobiol B*, vol. 98, no. 1, pp. 77-94, Jan 21 2010.
- [94] S. C. Davis, H. Dehghani, J. Wang, S. Jiang, B. W. Pogue, and K. D. Paulsen, "Image-guided diffuse optical fluorescence tomography implemented with Laplacian-type regularization," *Opt Express*, vol. 15, no. 7, pp. 4066-82, Apr 2 2007.
- [95] B. P. P. Yalavarthy, H. Dehghani, C. Carpenter, S. Jiang, and K. Paulsen, "Structural information within regularization matrices improves near infrared diffuse optical tomography," *Opt. Express*, vol. 15, pp. 8043-8058, 2007.
- [96] B. Brooksby *et al.*, "Magnetic resonance-guided near-infrared tomography of the breast," *Rev. of Sci. Inst.*, vol. 75, no. 12, pp. 5262-5270, 2004, doi: 10.1063/1.1819634.
- [97] Y. Lin, H. Gao, D. Thayer, A. L. Luk, and G. Gulsen, "Photo-magnetic imaging: resolving optical contrast at MRI resolution," (in eng), *Phys Med Biol*, vol. 58, no. 11, pp. 3551-62, Jun 7 2013, doi: 10.1088/0031-9155/58/11/3551.

- [98] Y. Lin, D. Thayer, A. Luk, and G. Gulsen, "Laser-Induced Photo-thermal Magnetic Imaging," *Applied Physics Letters*, vol. in press, 2012.
- [99] D. A. Thayer, Y. Lin, A. Luk, and G. Gulsen, "Laser-induced photo-thermal magnetic imaging," (in Eng), *Appl Phys Lett*, vol. 101, no. 8, p. 83703, Aug 20 2012, doi: 10.1063/1.4742158.
- [100] L. P. Gao and H., "Can we solve radiative transfer equation as fast as diffusion approximation?," in "BMES Annual Meeting," Hartford, 2011.
- [101] M. Schweiger and S. R. Arridge, "Comparison of two- and three-dimensional reconstruction methods in optical tomography," (in eng), *Appl Opt*, vol. 37, no. 31, pp. 7419-28, Nov 1 1998.
- [102] H. Erkol, F. Nouizi, A. Luk, M. B. Unlu, and G. Gulsen, "Comprehensive analytical model for CW laser induced heat in turbid media," *Optics Express*, vol. 23, no. 24, pp. 31069-31084, 2015.
- [103] A. T. Luk, S. Ha, F. Nouizi, D. Thayer, Y. Lin, and G. Gulsen, "A true multi-modality approach for high resolution optical imaging: photo-magnetic imaging," in *SPIE BiOS, 2014: International Society for Optics and Photonics*, pp. 89370G-89370G-7.
- [104] A. T. Luk, D. Thayer, Y. Lin, F. Nouizi, H. Gao, and G. Gulsen, "A novel high-resolution optical imaging modality: photo-magnetic imaging," in *SPIE BiOS, 2013: International Society for Optics and Photonics*, pp. 857404-857404-6.
- [105] F. Nouizi, A. Luk, D. Thayer, Y. Lin, S. Ha, and G. Gulsen, "Experimental validation of a high-resolution diffuse optical imaging modality: photomagnetic imaging," (in eng), *J Biomed Opt*, vol. 21, no. 1, p. 16009, Jan 2016, doi: 10.1117/1.JBO.21.1.016009.
- [106] F. Nouizi, M. Algarawi, H. Erkol, A. Luk, and G. Gulsen, "Multiwavelength photo-magnetic imaging algorithm improved for direct chromophore concentration recovery using spectral constraints," *Applied Optics*, vol. 60, no. 35, pp. 10855-10861, 2021.
- [107] M. Algarawi *et al.*, "Multi-Wavelength Photo-Magnetic Imaging System for Photothermal Therapy Guidance," *Lasers in Surgery and Medicine*, 2020.
- [108] M. Algarawi *et al.*, "Reconstruction chromophore concentration directly by Photo-Magnetic Imaging: simulation study," in *Optical Tomography and Spectroscopy, 2020: Optical Society of America*, p. JTU3A. 15.
- [109] M. Algarawi *et al.*, "Resolving tissue chromophore concentration at MRI resolution using multi-wavelength photo-magnetic imaging," *Biomedical Optics Express*, vol. 11, no. 8, pp. 4244-4254, 2020.
- [110] M. Algarawi *et al.*, "High-resolution chromophore concentration recovery using multi-wavelength photo-magnetic imaging," in *Multimodal Biomedical Imaging XIV, 2019*, vol. 10871: International Society for Optics and Photonics, p. 108710F.
- [111] F. Nouizi, H. Erkol, A. Luk, M. Algarawi, M. Mehrabi, and G. Gulsen, "Multi-wavelengths Photo Magnetic Imaging," in *Optical Tomography and Spectroscopy, 2018: Optical Society of America*, p. JW3A. 45.
- [112] A. Luk, F. Nouizi, H. Erkol, M. B. Unlu, and G. Gulsen, "Ex vivo validation of photo-magnetic imaging," *Optics letters*, vol. 42, no. 20, pp. 4171-4174, 2017.
- [113] A. T. Luk, F. Nouizi, M. Marks, T. Kart, and G. Gulsen, "Monitoring gold nanoparticle distribution with high resolution using photo-magnetic imaging," in

- Optical Interactions with Tissue and Cells XXVII*, 2016, vol. 9706: International Society for Optics and Photonics, p. 97060M.
- [114] F. Nouizi, H. Erkol, A. Luk, M. Marks, M. B. Unlu, and G. Gulsen, "An accelerated photo-magnetic imaging reconstruction algorithm based on an analytical forward solution and a fast Jacobian assembly method," (in ENG), *Phys Med Biol*, vol. 61, no. 20, pp. 7448-7465, Oct 2016, doi: 10.1088/0031-9155/61/20/7448.
 - [115] F. Nouizi, H. Erkol, A. Luk, Y. Lin, and G. Gulsen, "Analytical Photo Magnetic Imaging," in *Optical Tomography and Spectroscopy*, 2016: Optical Society of America, p. OW4D. 7.
 - [116] F. Nouizi, H. Erkol, A. Luk, M. B. Unlu, and G. Gulsen, "Real-time photo-magnetic imaging," *Biomedical Optics Express*, vol. 7, no. 10, pp. 3899-3904, 2016.
 - [117] B. Brooksby *et al.*, "Imaging breast adipose and fibroglandular tissue molecular signatures by using hybrid MRI-guided near-infrared spectral tomography," *Proc Natl Acad Sci U S A*, vol. 103, no. 23, pp. 8828-33, Jun 6 2006.
 - [118] F. El-Ghussein, M. A. Mastanduno, S. Jiang, B. W. Pogue, and K. D. Paulsen, "Hybrid photomultiplier tube and photodiode parallel detection array for wideband optical spectroscopy of the breast guided by magnetic resonance imaging," (in eng), *J Biomed Opt*, vol. 19, no. 1, p. 011010, Jan 2014, doi: 10.1117/1.JBO.19.1.011010.
 - [119] T. D. O'Sullivan *et al.*, "Optical imaging correlates with magnetic resonance imaging breast density and reveals composition changes during neoadjuvant chemotherapy," (in Eng), *Breast Cancer Res*, vol. 15, no. 1, p. R14, Feb 22 2013, doi: 10.1186/bcr3389.
 - [120] Y. Lin, D. Thayer, O. Nalcioglu, and G. Gulsen, "Tumor characterization in small animals using magnetic resonance-guided dynamic contrast enhanced diffuse optical tomography," (in eng), *J Biomed Opt*, Research Support, N.I.H., Extramural Research Support, Non-U.S. Gov't vol. 16, no. 10, p. 106015, Oct 2011, doi: 10.1117/1.3643342.
 - [121] S. C. Davis *et al.*, "Magnetic resonance--coupled fluorescence tomography scanner for molecular imaging of tissue," *Review of Scientific Instruments*, vol. 79, no. 6, pp. 064302-10, 2008, doi: 10.1063/1.2919131.
 - [122] Y. Lin, "Temperature modulated fluorescence tomography in a turbid media ", ed: Applied Physics Letters, 2012.
 - [123] M. Mehrabi *et al.*, "CCD-based temperature modulated fluorescence tomography," in *Optical Tomography and Spectroscopy of Tissue XIII*, 2019, vol. 10874: International Society for Optics and Photonics, p. 108740Y.
 - [124] F. Nouizi, T. Kwong, Y. Lin, U. Sampathkumaran, A. Shaaz, and G. Gulsen, "A combined HIFU-Fluorescence Tomography high-resolution imaging technique using temperature-modulated thermdots," in *Optical Trapping Applications*, 2013: Optical Society of America, p. JW3B. 8.
 - [125] Y. Lin, T. C. Kwong, L. Bolisay, and G. Gulsen, "Temperature-modulated fluorescence tomography based on both concentration and lifetime contrast," (in eng), *J Biomed Opt*, vol. 17, no. 5, p. 056007, May 2012, doi: 10.1117/1.JBO.17.5.056007.
 - [126] Y. Lin, L. Bolisay, M. Ghijsen, T. C. Kwong, and G. Gulsen, "Temperature-modulated fluorescence tomography in a turbid media," (in ENG), *Appl Phys Lett*, vol. 100, no. 7, pp. 73702-737024, Feb 2012, doi: 10.1063/1.3681378.

- [127] R. C. a. W. R. E. Gonzalez, *Digital Image Processing (3rd Edition)*. USA: Prentice-Hall Inc., 2006.
- [128] R. O. Duda and P. E. Hart, "Use of the Hough transformation to detect lines and curves in pictures," *Communications of the ACM*, vol. 15, no. 1, pp. 11-15, 1972.
- [129] D. H. Ballard, "Generalizing the Hough transform to detect arbitrary shapes," *Pattern recognition*, vol. 13, no. 2, pp. 111-122, 1981.
- [130] S. J. K. Pedersen, "Circular Hough Transform," in *Encyclopedia of Biometrics*, 2009.
- [131] S. Haykin, "Neural Networks and Learning Machines," 2010.
- [132] N. Altman and M. Krzywinski, "Simple linear regression," *Nature Methods*, vol. 12, no. 11, pp. 999-1000, 2015/11/01 2015, doi: 10.1038/nmeth.3627.
- [133] H. Borchani, G. Varando, C. Bielza, and P. Larranaga, "A survey on multi-output regression," *Wiley Interdisciplinary Reviews: Data Mining and Knowledge Discovery*, vol. 5, no. 5, pp. 216-233, 2015.
- [134] S. Jadon, "A survey of loss functions for semantic segmentation," 2020.
- [135] Z. Zhang and M. Sabuncu, "Generalized cross entropy loss for training deep neural networks with noisy labels," *Advances in neural information processing systems*, vol. 31, 2018.
- [136] T.-Y. Lin, P. Goyal, R. Girshick, K. He, and P. Dollár, "Focal loss for dense object detection," in *Proceedings of the IEEE international conference on computer vision*, 2017, pp. 2980-2988.
- [137] F. Rosenblatt, "The perceptron: a probabilistic model for information storage and organization in the brain," *Psychological review*, vol. 65, no. 6, p. 386, 1958.
- [138] K. Ikemura and F. Nouzi, "Convolutional Neural Network to Classify Histological Images: Idea on How to Increase Sample Size," in *LABORATORY INVESTIGATION*, 2018, vol. 98: NATURE PUBLISHING GROUP 75 VARICK ST, 9TH FLR, NEW YORK, NY 10013-1917 USA, pp. 589-590.
- [139] A. Eresen *et al.*, "Early assessment of irreversible electroporation ablation outcomes by analyzing MRI texture: preclinical study in an animal model of liver tumor," *American Journal of Translational Research*, vol. 14, no. 8, p. 5541, 2022.
- [140] J. Du, "Understanding of object detection based on CNN family and YOLO," in *Journal of Physics: Conference Series*, 2018, vol. 1004: IOP Publishing, p. 012029.
- [141] Y. Zhang *et al.*, "Prediction of Neoadjuvant Chemoradiation Therapy Response in Rectal Cancer Using Radiomics Compared to Deep Learning Based on Pre-Treatment and mid-RT MRI," in *Proc. Intl. Soc. Mag. Reson. Med*, 2019, vol. 27, p. 0101.
- [142] R. Mutegeki and D. S. Han, "A CNN-LSTM approach to human activity recognition," in *2020 international conference on artificial intelligence in information and communication (ICAIIIC)*, 2020: IEEE, pp. 362-366.
- [143] Y. Zhang *et al.*, "Deep Learning Approaches Using Convolutional Neural Networks to Generate Synthetic CT from Spinal MRI for Radiotherapy Planning."
- [144] S.-i. Amari, "Backpropagation and stochastic gradient descent method," *Neurocomputing*, vol. 5, no. 4-5, pp. 185-196, 1993.
- [145] J. Canny, "A computational approach to edge detection," *IEEE Transactions on pattern analysis and machine intelligence*, no. 6, pp. 679-698, 1986.